

## Probing Europa's interior with natural sound sources

Sunwoong Lee,<sup>a</sup> Michele Zanolin,<sup>a</sup> Aaron M. Thode,<sup>a</sup> Robert T. Pappalardo,<sup>b</sup>  
and Nicholas C. Makris<sup>a,\*</sup>

<sup>a</sup> Department of Ocean Engineering, Massachusetts Institute of Technology, 77 Massachusetts Avenue, Room 5-222, Cambridge, MA 02139, USA

<sup>b</sup> Laboratory for Atmospheric and Space Physics, University of Colorado, Campus Box 392, Boulder, CO 80309-0392, USA

Received 24 December 2002; revised 26 April 2003

### Abstract

Europa's interior structure may be determined by relatively simple and robust seismo-acoustic echo sounding techniques. The strategy is to use ice cracking events or impacts that are hypothesized to occur regularly on Europa's surface as sources of opportunity. A single passive geophone on Europa's surface may then be used to estimate the thickness of its ice shell and the depth of its ocean by measuring the travel time of seismo-acoustic reflections from the corresponding internal strata. Quantitative analysis is presented with full-field seismo-acoustic modeling of the Europan environment. This includes models for Europan ambient noise and conditions on signal-to-noise ratio necessary for the proposed technique to be feasible. The possibility of determining Europa's ice layer thickness by surface wave and modal analysis with a single geophone is also investigated.

© 2003 Elsevier Inc. All rights reserved.

*Keywords:* Europa, interiors; Ices; Tides; Tectonics; Ocean; Acoustic, seismic

### 1. Introduction

Our goal is to show how Europa's interior structure may be revealed by relatively simple and robust seismo-acoustic echo-sounding techniques using natural sources of opportunity. Echo sounding is the traditional and most widely used tool to chart the depth and composition of terrestrial oceans and sub-ocean layers (Medwin and Clay, 1998). It employs an active acoustic source and passive receiver to measure the arrival time and amplitude of reflections from the layers to be charted. Our Europan strategy differs from the terrestrial one in that the primary source of sound is not controlled. Rather, it is proposed to arise from ice cracking events and impacts hypothesized to occur regularly on Europa's surface. A single passive geophone on Europa's surface may then be used to estimate (1) its range from a natural source event by analysis of direct compressional and shear wave arrivals in the ice, and (2) the thickness of the ice shell and depth of the ocean by travel time analysis of specular reflections from the corresponding internal strata. The technique, however, requires the ice-crack or impact event of opportunity to be sufficiently

energetic for its reflections to stand above the ambient noise generated by other more distant or less energetic events.

To help quantitatively explore the issues involved in echo-sounding, and other seismo-acoustic techniques for probing Europa's interior, our analysis proceeds together with the development of a full-field seismo-acoustic model for Europa. This includes analysis of ice-cracking and impact source events, seismo-acoustic propagation in Europa's stratified environment, and Europan ambient noise. Here we follow the common convention of referring to both compressional and shear wave disturbances in solids, such as Europa's outer ice shell and interior mantle, as "seismic waves," and compressional waves in fluids, such as Europa's potential ocean, as "acoustic waves." By this convention, waves that propagate from ice to water or vice-versa, for example, are referred to as "seismo-acoustic waves."

Our interest in this problem stems from the significant amount of evidence collected by the Galileo Probe in the past decade to support the possibility that an ocean of liquid water may lie beneath Europa's exterior icy surface. Induced magnetic field measurements (Khurana et al., 1998) suggest the existence of a conducting layer beneath the ice surface that is at least a few kilometers thick and likely corresponds to a liquid ocean of salty water. Various researchers have argued that many of the morphological features that char-

\* Corresponding author.

E-mail address: [makris@mit.edu](mailto:makris@mit.edu) (N.C. Makris).

acterize Europa's icy surface can best be explained by the presence of an ocean of liquid water below (Pappalardo et al., 1998). This is put in context by the conclusion of Anderson et al. (1998) that the total thickness of ice and potentially liquid water on Europa's surface is between 80 to 170 km, based on gravity data. Together these observations provide compelling but inconclusive evidence for a subsurface European ocean leaving the thickness of the outer ice shell and the depth of the potential ocean poorly constrained.

A variety of techniques have been proposed to measure the thickness of Europa's outer ice shell. They involve measurement of crater morphology (Schenk, 2002), tidal gravity (Greenberg, 2002; Anderson et al., 1998; Wu et al., 2001), laser altimetry (Cooper et al., 2002), ice-penetrating radar reflections (Chyba et al., 1998; Moore, 2000), and ice-bourne seismic wave interference and dispersion (Kovach and Chyba, 2001). All but the last have the advantage of being achievable by either fly-by or orbital rather than landing missions. While each may indicate the presence of an ocean, none are sensitive to its thickness (Cooper et al., 2002).

Only two techniques are currently available to remotely determine the thickness of a deep ocean layer on Europa. The first involves extensive magnetometer measurements by a low flying orbiter (Khurana et al., 1998; Kivelson et al., 1999, 2000). These measurements, however, cannot determine the location of the ocean layer or its structure. The other is the echo-sounding technique under discussion, the primary advantage of which is its ability to determine the absolute interior structure of both the ice and potential ocean layers. A potential disadvantage is that it requires a landing mission.

The first European landing mission will likely carry only a single triaxial geophone capable of measuring seismo-acoustic displacements in three spatial dimensions at a single point on Europa's surface. Besides echo-sounding, listening for audible signs of life, and potentially inferring and categorizing dynamical processes of the ice by their acoustic signatures, an initial task for this sensor could be to determine the overall level of seismo-acoustic activity on Europa by time series and spectral analysis. Correlations could be made of ambient noise versus environmental stress level to determine whether noise levels respond directly to orbital eccentricities. Such an analysis was conducted for the Earth's Arctic Ocean where roughly two meters of nearly continuous pack ice cover an ocean that is typically between 0.1 and 5 km in depth. These terrestrial results show a near perfect correlation between underwater noise level and environmental stresses and moments applied to the ice sheet from wind, current, and drift (Makris and Dyer 1986, 1991). Additionally, in the Antarctic, both the flexural motion of ice shelves and the level of seismicity due to tidally induced ice-fracturing events are correlated with the sea tide (Robin, 1958).

For Europa, Hoppa et al. (1999) show that environmental stresses due to tidal forces vary significantly over the period of its eccentric 3.5 day orbital period and that these stresses

may lead to the near daily formation of cycloidal arcs similar to those observed to extend over hundreds of kilometers on Europa's surface. Based on the maximum tidal surface stress expected by Hoppa et al. (1999) and basic concepts from fracture mechanics, we show that a given cycloidal arc is likely to be formed as a sequence of hundreds of discrete and temporally disjoint cracking events.

A combination of factors, such as the interplay of diurnal stresses with inhomogeneities in the outer ice shell or its potential asynchronous rotation due to an ocean layer below (Leith and McKinnon, 1996), may lead to "Big Bang" cracking events. These events would be statistically less frequent but much more energetic than those primarily caused by diurnal stresses in pure ice. Echo returns from Big Bang events would be more likely to stand above the ambient noise and so make echo sounding for Europa's interior structure more practical. We determine the tensile stresses and crack depths necessary to generate Big Bang events. We also show that even small impactors, in the 1–10-m radius range, fall into the Big Bang category, and that Big Bang events will radiate spectral energy peaking in the roughly 1- to 10-Hz range. This is significant because the corresponding seismo-acoustic wavelengths in ice and water will range from hundreds to thousands of meters. Such long wavelength disturbances suffer minimal attenuation from mechanical relaxation mechanisms in ice and water and are relatively insensitive to shadowing by similarly sized anomalies in the ice or on the seafloor that could severely limit remote sensing techniques that rely on shorter wavelengths.

## 2. Modeling Europa as a stratified seismo-acoustic medium

We begin our analysis by establishing models for Europa as a stratified medium for seismo-acoustic wave propagation. These models specify compressional wave speed  $c_p$ , shear wave speed  $c_s$ , compressional wave attenuation  $\alpha_p$ , shear wave attenuation  $\alpha_s$ , and density  $\rho$  as a function of depth on Europa.

There are two canonical models of Europa's interior structure. The first is the rigid ice shell model, where heat transport is achieved by conduction throughout a completely brittle and elastic ice-shell (Ojakangas and Stevenson, 1989; Greenberg et al., 1998). The second is the convective ice shell model, where heat is transported primarily by convection of warm ice at the base that can become buoyant enough to rise toward the surface (Pappalardo et al., 1998; McKinnon, 1999; Deschamps and Sotin, 2001).

Linearized internal temperature profiles for these two models are shown in Fig. 1(a). The resulting temperature profiles are used to construct compressional and shear wave speed profiles in the ice by the methods described in Appendix A. The rigid ice shell model is characterized by an almost linear temperature change from the top of the ice shell to the ice–water interface, whereas the convective ice shell model

Table 1  
Seismo-acoustic parameters

Material	$c_p$ (m/s)	$c_s$ (m/s)	$\alpha_p$ (dB/ $\lambda$ )	$\alpha_s$ (dB/ $\lambda$ )	$\rho$ (kg/m <sup>3</sup> )
Ice	see Appendix A	see Appendix A	0.24	0.72	930
Water	see Chen and Millero (1977)		0.01		1000
Sediment	1575	80	1.0	1.5	1050
Basalt	5250	2500	0.1	0.2	2700

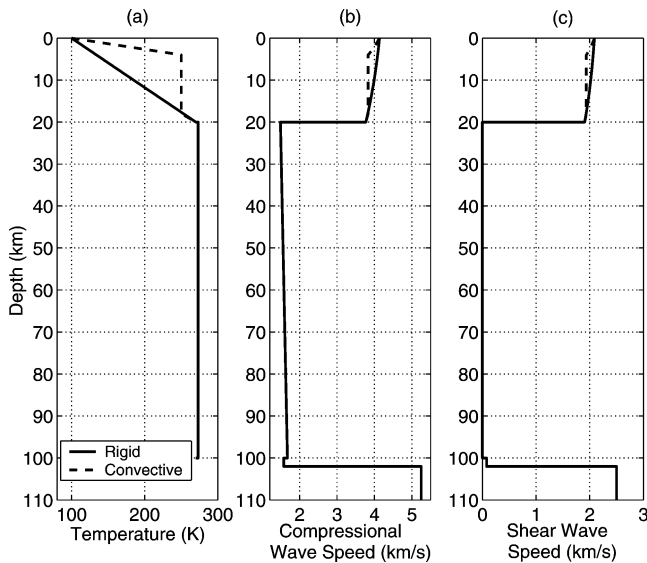


Fig. 1. Temperature, compressional wave speed, and shear wave speed profiles for 20 km thick rigid and convective ice shell models. The solid and dashed lines represent the rigid and convective ice shell models, respectively.

leads to a strong temperature gradient on top and bottom of the ice shell, and a mild temperature gradient in the middle. In the latter, temperature is assumed to increase with depth from an average surface value of 100 K (Orton et al., 1996; Spencer et al., 1999) to 250 K in the upper thermal boundary layer, which is assumed to comprise the upper 20% of the ice shell, remain constant for the bulk of ice shell before finally increasing to 260 K in the lower thermal boundary layer, which is assumed to comprise the lower 10% of the ice shell.

The sound speed of sea water is mainly a function of temperature, pressure, and salinity. Several regression equations are available to estimate sound speed from these variables. Here we employ one valid under high pressure (Chen and Millero, 1977) to estimate the sound speed profile in a sub-surface European ocean. This ocean is assumed to have a salinity of roughly 3.5%, similar to terrestrial oceans (Khurana et al., 1998), and a temperature of roughly 273 K, the melting temperature of ice in the terrestrial environment.

The mantle beneath the ocean is assumed to be comprised of a 2-km of sediment layer overlying a basalt halfspace. The sediment is taken to have sound speed and density similar to water as in terrestrial oceans.

In our subsequent simulations and analysis, we consider four European sound speed profiles based upon 5-km rigid,

20-km rigid, 20-km convecting, and 50-km convecting ice shell models. The assumed compressional and shear wave speed profiles through the ice, water and mantle are shown in Fig. 1(b) and (c) for both 20-km models. Assumed seismo-acoustic parameters of the medium common to all models are shown in Table 1.

Attenuation increases significantly with frequency in terrestrial sea ice, water and sediment. The attenuation values shown in Table 1, given in standard decibel units per wavelength, are valid in the roughly 1–4-Hz range of the spectral peak of a hypothesized Big Bang ice-quake event used in the simulations to follow. Ice attenuation values are extrapolated to below 200 Hz from the linear trend observed in Arctic Ocean ice (McCammon and McDaniel, 1985). Attenuation due to volumetric absorption in a potential European ocean is taken to be similar to that in terrestrial seawater, which is relatively insignificant in the low frequency range of interest in the present study (Urlick, 1983). Attenuations in the sediment and basalt assumed for the mantle also follow terrestrial analogs which are far more significant than that found in seawater.

A schematic of Europa as a stratified seismo-acoustic medium is given in Fig. 2 for a convective ice shell. In the rigid ice shell, the upper thermal boundary layer would continue to the ice-ocean interface, eliminating the other two ice layers shown.

### 3. Source mechanisms and characteristics

Our primary interest is in source events that are both energetic enough and frequent enough for the proposed echo-sounding technique to be feasible within the period of a roughly week to month long European landing mission. Source events of opportunity must have sufficient energy for their echo returns from the ice–water and water–mantle interfaces to stand above the accumulated ambient noise of other more distant or weaker sources. We proceed by first estimating the seismo-acoustic energy spectrum of ice-cracking sources and then impact sources.

#### 3.1. Ice-cracking

Surface cracking events are expected to occur in the brittle, elastic layer of Europa's outer ice shell in response to tensile stresses arising from a diverse set of mechanisms. We show that the source time dependence and energy spectrum

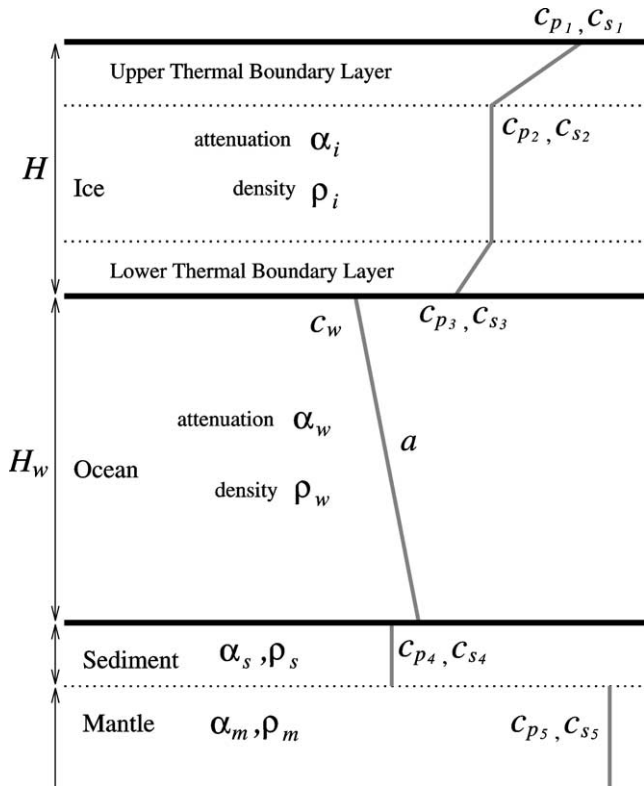


Fig. 2. Schematic diagram of the full Europa model for a convective ice shell. In the wave speed profile,  $c_p$ ,  $c_s$  are compressional and shear wave speeds in elastic media,  $c_w$  is the acoustic wave speed in the ocean,  $a$  is the sound speed gradient in the ocean.  $H$  and  $H_w$  are the thicknesses of the ice shell and subsurface ocean.  $\alpha$  and  $\rho$  are the attenuation and density of the media.

can be estimated from crack depth. Expected crack depths can in turn be estimated from the imposed tensile stress.

The maximum depth  $h$  of a surface crack is estimated to occur where tensile stress  $\sigma$  is balanced by the pressure due to the gravitational overburden of the ice shell (Crawford and Stevenson, 1988; Weertman 1971a, 1971b; Muller and Muller, 1980),

$$\sigma \sim \rho_i g h, \quad (1)$$

where  $g = 1.3 \text{ m/s}^2$  is the gravitational acceleration on Europa's surface.

Europa's roughly 3.5 day eccentric jovian orbit is expected to lead to a significant diurnally varying tidal stress, with maximum values ranging from 40 kPa (Hoppa et al., 1999) to 100 kPa (Leith and McKinnon, 1996) if a subsurface ocean of at least a few kilometers thickness is present. Over much longer time scales of roughly 10 Myr, the nonsynchronous rotation of an outer ice shell decoupled from the mantle by a subsurface ocean could lead to maximum tensile stresses as large as 8 MPa (Leith and McKinnon, 1996).

The flexural strength of terrestrial sea ice was measured as a function of brine volume (Weeks and Cox, 1984). Based on this work, we estimate a brine volume of 23% is necessary to crack terrestrial ice with the applied surface stress of

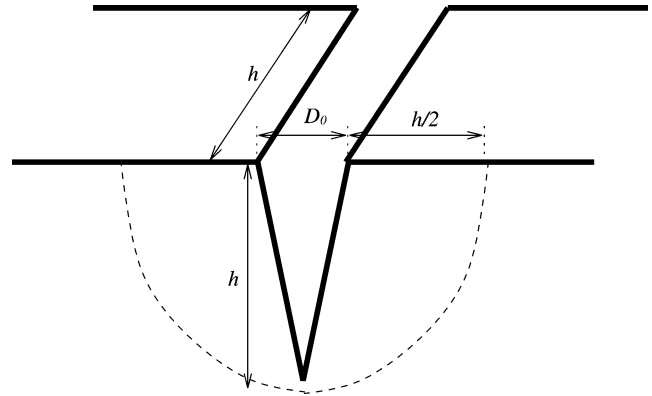


Fig. 3. The geometry of surface tensile cracks. A crack with depth  $h$  propagates until the opening length is  $h$ .  $D_0$  is the opening width of a crack. The volume within the dotted line is the regime where the tensile stress is released by the crack.

40 kPa computed for Europa by Hoppa et al. (1999). This is higher than the terrestrial value which usually varies between 1 to 15%. The flexural strength of ice on Europa's surface is expected to be higher than that on Earth due to Europa's much lower surface temperature. However, by assuming that flexural strength is proportional to Young's modulus and considering Appendix A, the flexural strength will only increase by roughly 20% which still puts the brine volume estimated to be roughly 23% on Europa's surface.

The most frequent type of cracking events, expected to occur daily with the diurnal tide, should then penetrate to roughly 50-m depths, based on the maximum tensile stress given by Hoppa et al. (1999), or to 150-m depths based upon the analysis of Leith and McKinnon. Less frequent events due to asynchronous rotation can penetrate to depths well beyond 1 km (Leith and McKinnon, 1996). The interplay between short term diurnal stresses, local ice inhomogeneities and even small asynchronous rotations (Greeley et al., 2003), could lead to a reasonable frequency of local Big Bang cracking events, here defined as those exceeding 150-m depths, over the roughly month long period of a first European landing mission.

A detailed derivation of the seismo-acoustic energy spectrum for a tensile crack as a function of depth  $h$  is provided in Appendix C.1 where the crack geometry is shown in Fig. 3. In this derivation it is conservatively assumed that cracks do not exceed a minimum length of  $h$  (Aki and Richards, 1980; Farmer and Xie, 1989). The crack width  $D_0$  can be determined by

$$\sigma = E \varepsilon \simeq E \frac{D_0}{h}. \quad (2)$$

With the gravitational overburden assumption, we expect

$$D_0 \simeq \frac{\sigma h}{E} \simeq \frac{\rho g h^2}{E}, \quad (3)$$

where  $E = 10 \text{ GPa}$  is Young's modulus for pure ice, as given in Appendix A. The pure ice assumption leads to a conservative estimate of the crack opening width. Note, however,

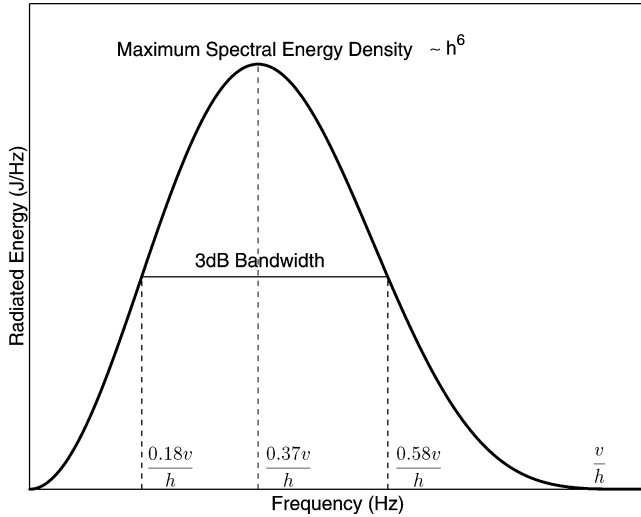


Fig. 4. The radiated seismo-acoustic energy spectrum  $\epsilon(f)$  defined by Eqs. (C.9) and (C.41) as a function of crack depth  $h$ . The amplitude of the spectrum is proportional to  $h^6$ , and the peak frequency and bandwidth are inversely proportional to  $h$ .

that the choice of Young’s modulus does not change the relative energy levels between the cracks of various depths, and the signal-to-noise ratio analysis in this paper remains valid.

The crack is also assumed to open as a linear function of time over a period equal to the maximum crack width over the crack propagation speed, as shown in Fig. C.1. The crack propagation speed is taken to be

$$v \simeq 0.9c_s, \tag{4}$$

following standard models of fracture mechanics (Aki and Richards, 1980) and experimental measurements of cracks on ice at terrestrial temperatures (Lange and Ahrens, 1983; Stewart and Ahrens, 1999). The opening time of the crack is then directly proportional to the crack depth  $h$ .

The source energy spectrum for a general crack of depth  $h$  is given in Fig. 4, from which it can be seen that the frequency of the peak and 3-dB bandwidth are inversely proportional to crack depth  $h$  while the peak energy spectral density grows with a dramatic  $h^6$  proportionality. This is illustrated in Fig. 5, where source energy spectral levels are given for various crack depths and it is clear that Big Bang events, with depths exceeding 150-m depths, will be at least  $3^6$  times more energetic than the nominal 50-m deep cracks expected solely from diurnal tides.

From Eq. (3), the opening widths of the cracks will be 0.3 mm and 8 mm for 50-m and 250-m cracks, respectively. Such small-scale surface motions and feature changes will not be readily observable from orbit, but could easily be detected by seismo-acoustic sensors.

### 3.2. Impacts

The rate of small impacts on Europa, for impactors in the 1–10-m radius range, is poorly constrained. A recent model predicts a rate of 0.2 to 16 for such impacts per year over

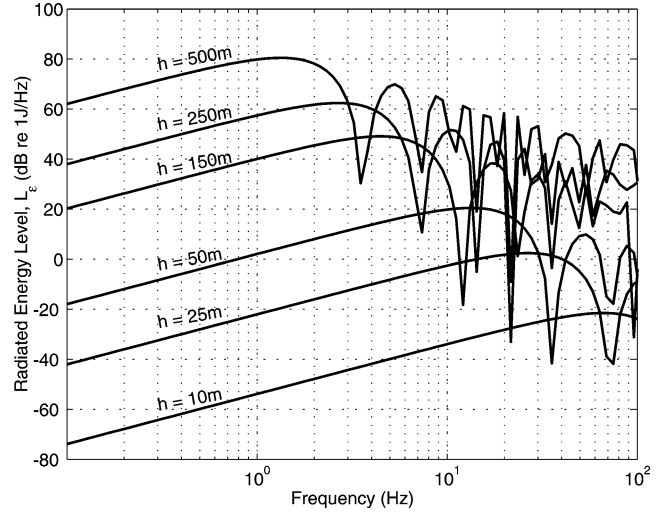


Fig. 5. The radiated energy level  $L_\epsilon$  from surface cracks for various crack depths  $h$ , as defined in Eq. (C.42).

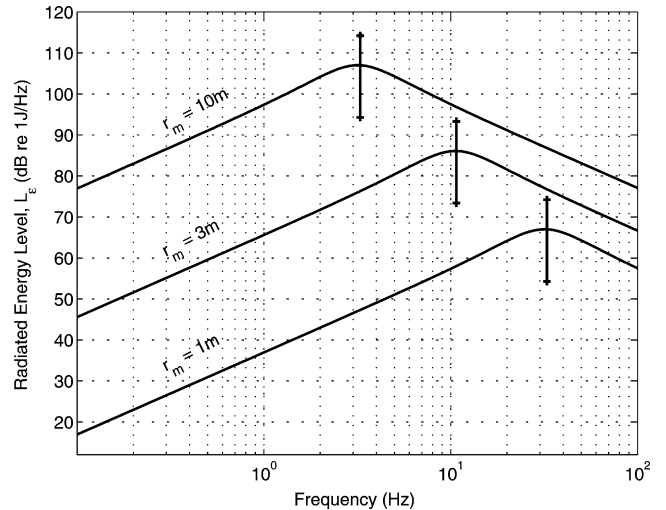


Fig. 6. The radiated energy level  $L_\epsilon$  for various radii  $r_m$  of impactors, as defined in Eq. (C.56). Solid lines represent energy levels of rock impactors with density  $\rho = 3 \text{ g/cm}^3$  and impact velocity  $v = 20 \text{ km/s}$ . Energy levels of iron meteors with  $\rho = 7 \text{ g/cm}^3$  and  $v = 30 \text{ km/s}$ , and those of comets with  $\rho = 1 \text{ g/cm}^3$  and  $v = 8 \text{ km/s}$  are also shown as errorbars in the figure.

the entire satellite (Bierhaus et al., 2001; personal communication with E.B. Bierhaus). To determine the source energy spectrum for impacts as a function of impactor size, composition and speed, we make use of the impact-explosion analogy discussed in Melosh (1989). A derivation of the radiated energy spectrum using underground explosion phenomenology is given in Appendix C.2.

The radiated energy spectral levels for impactors of various radii are shown in Fig. 6, assuming a nominal rock meteor with  $3 \text{ g/cm}^3$  density and  $20 \text{ km/s}$  impact velocity. This energy level will vary within  $\pm 10 \text{ dB}$  depending on the seismic efficiency discussed in Appendix C.2.

Small impacts, then may provide another source of Big Bang events that have energies well above those expected solely from tensile cracks driven by diurnal tides and may

be frequent enough to be used as sources of opportunity for echo-sounding.

#### 4. Seismo-acoustic wave propagation on Europa

The radiated field from tensile cracks typically have directionality, but here we assume that an omnidirectional source, or a monopole, should best describe the expected or average directionality.

Assuming a time-harmonic acoustic field at frequency  $f$ , the equation of motion in horizontally stratified, homogeneous, isotropic elastic media can be expressed in cylindrical coordinates  $(r, z)$  as (Schmidt and Tango, 1986)

$$\begin{aligned} \dot{u}_m(r, z, f) &= -i2\pi f S(f) \left[ \frac{\partial}{\partial r} G_{\phi, m}(r, z, f) \right. \\ &\quad \left. + \frac{\partial^2}{\partial r \partial z} G_{\psi, m}(r, z, f) \right] \\ &\equiv S(f) G_{\dot{u}, m}(r, z, f), \end{aligned} \quad (5)$$

$$\begin{aligned} \dot{w}_m(r, z, f) &= -i2\pi f S(f) \left[ \frac{\partial}{\partial z} G_{\phi, m}(r, z, f) \right. \\ &\quad \left. - \frac{1}{r} \frac{\partial}{\partial r} r \frac{\partial}{\partial r} G_{\psi, m}(r, z, f) \right] \\ &\equiv S(f) G_{\dot{w}, m}(r, z, f), \end{aligned} \quad (6)$$

where  $\{\dot{u}_m, \dot{w}_m\}$  are the radial and vertical velocity components,  $\{G_{\phi, m}, G_{\psi, m}\}$  are solutions to compressional (P) and shear vertical (SV) displacement potential Helmholtz equations in each layer  $m$  with corresponding compressional wave speed  $c_{p, m}$  and shear wave speed  $c_{s, m}$ , and  $S(f)$  is the spectral amplitude of volume injection by the source at frequency  $f$ .

The solutions are composed of the homogeneous and inhomogeneous solutions of the Helmholtz equations,

$$G_{\phi, m} = \tilde{G}_{\phi, m} + \hat{G}_{\phi, m}, \quad (7)$$

$$G_{\psi, m} = \tilde{G}_{\psi, m} + \hat{G}_{\psi, m}. \quad (8)$$

The homogeneous solutions satisfy

$$[\nabla^2 + k_m^2] \tilde{G}_{\phi, m}(r, z, f) = 0, \quad (9)$$

$$[\nabla^2 + \kappa_m^2] \tilde{G}_{\psi, m}(r, z, f) = 0, \quad (10)$$

where  $k_m = 2\pi f/c_{p, m}$  and  $\kappa_m = 2\pi f/c_{s, m}$  are wavenumbers of compressional and shear waves. The homogeneous solutions can be expressed in the wavenumber domain using integral representations,

$$\begin{aligned} \tilde{G}_{\phi, m}(r, z, f) &= \int_0^{\infty} [A_m^- e^{-ik_{z, m} z} + A_m^+ e^{ik_{z, m} z}] \\ &\quad \times J_0(k_r r) k_r dk_r, \end{aligned} \quad (11)$$

$$\begin{aligned} \tilde{G}_{\psi, m}(r, z, f) &= \int_0^{\infty} [B_m^- e^{-i\kappa_{z, m} z} + B_m^+ e^{i\kappa_{z, m} z}] \\ &\quad \times J_0(k_r r) dk_r, \end{aligned} \quad (12)$$

where  $J_0$  is the Bessel function of the first kind,  $k_r$  is the horizontal wavenumber, and

$$k_{z, m} = \sqrt{k_m^2 - k_r^2}, \quad (13)$$

$$\kappa_{z, m} = \sqrt{\kappa_m^2 - k_r^2}, \quad (14)$$

are the vertical wavenumbers.

The inhomogeneous Helmholtz equation with a monopole source at  $r = 0, z = z'$ ,

$$[\nabla^2 + k_m^2] \hat{G}_{\phi, m}(r, z, z', f) = -\frac{\delta(r)}{2\pi r} \delta(z - z') \quad (15)$$

has solution in the form of the integral representation

$$\hat{G}_{\phi, m}(r, z, z', f) = -\frac{1}{4\pi} \int_0^{\infty} \frac{e^{ik_{z, m}|z-z'|}}{ik_{z, m}} J_0(k_r r) k_r dk_r. \quad (16)$$

The inhomogeneous solution for SV component  $\hat{G}_{\psi, m}$  is zero, since an omnidirectional source does not excite SV component.

Two-dimensional simulations including radial and vertical components are sufficient since out-of-plane motion does not occur for the assumed monopole source. A stable numerical solution in the frequency domain is obtained by wavenumber integration (Schmidt and Tango, 1986; Kim, 1989). The time domain solution and synthetic seismograms are then obtained by Fourier synthesis.

In this section, we investigate wave propagation in Europa through transmission loss, time-range, and synthetic seismogram analysis.

##### 4.1. Transmission loss

Transmission loss is a measure of the acoustic field level as a function of position, and is calculated in the frequency domain for a time-harmonic source via

$$\begin{aligned} \text{TL}_{\dot{u}}(\mathbf{r}, \mathbf{r}') &= -20 \log_{10} \frac{|\dot{u}(\mathbf{r}, \mathbf{r}')|}{|\dot{\mathbf{v}}_0(\mathbf{r}')|} \text{ dB re } r_{\text{ref}}, \\ \text{TL}_{\dot{w}}(\mathbf{r}, \mathbf{r}') &= -20 \log_{10} \frac{|\dot{w}(\mathbf{r}, \mathbf{r}')|}{|\dot{\mathbf{v}}_0(\mathbf{r}')|} \text{ dB re } r_{\text{ref}}, \end{aligned} \quad (17)$$

where  $\dot{u}(\mathbf{r}, \mathbf{r}')$  and  $\dot{w}(\mathbf{r}, \mathbf{r}')$  are the horizontal and vertical velocity fields at point  $\mathbf{r}$  for a source at point  $\mathbf{r}'$ , and  $\dot{\mathbf{v}}_0(\mathbf{r}')$  is the velocity produced at a distance of  $r_{\text{ref}} = 1$  m from the same source in an infinite, homogeneous medium with density  $\rho(\mathbf{r}')$  and compressional wave speed  $c_p(\mathbf{r}')$ .

The magnitudes of the vertical and horizontal particle velocities of an ice source 50-m below the ice-vacuum interface in the 20-km convecting ice shell model are shown in Fig. 7 at 2-Hz frequency, corresponding to the central frequency typical in a Big Bang source event. This figure shows the transmission and reflection of acoustic waves from the ice–water and water–mantle interfaces at up to 200-km range. Fringes in the source radiation pattern due to the free surface boundary condition at the ice-vacuum interface

are visible as are modal interference patterns in the ice layer. These patterns are a function of frequency, and are not readily observable for a typical broadband ice-crack or impact source. As expected, the horizontal particle velocity field in the ocean directly beneath the source is very weak due to the almost total reflection of the shear wave at the ice–water interface, which cannot support horizontal shear.

Figure 7 illustrates how efficiently seismic waves propagate through the ice shell as do acoustic waves through the subsurface ocean, and how a geophone located at the top of the ice shell will be able to detect multiple reflections from the ice–water interface as well as the water–mantle interface.

The Rayleigh wave is a surface wave that travels at roughly 90% of the medium shear speed for a homogeneous halfspace, and suffers only cylindrical spreading in horizontal range but is attenuated exponentially with depth from the surface it travels on. It will be strongly excited on the ice–vacuum interface by sources of shallow depth, such as surface cracking events, impacts and the near-surface source of the given example. It can be seen in Fig. 7 as a strong vertical velocity field trapped near the surface. Characteristic differences between the Rayleigh wave and direct compressional wave arrivals will prove to be useful in determining the range of surface sources of opportunity. The frequency-dependent characteristics of a Rayleigh wave may also be used as another possible tool to probe the interior structure of the ice shell, and will be described in Section 7.2. If the wavelength of the Rayleigh wave is long compared to the thickness of the ice shell, it will propagate as a flexural wave on a thin plate.

4.2. Nomenclature of acoustic rays

The analysis of seismo-acoustic wave propagation from a source to receiver can be intuitively understood by applying ray theory which is valid when the wavelength is small compared to variations in the medium. Rays are defined as a family of curves that are perpendicular to the wavefronts emanating from the source, and are obtained by solving the eikonal equation (Brekhovskikh and Lysanov, 1982; Frisk, 1994; Medwin and Clay, 1998).

In order to describe the various seismo-acoustic rays propagating in ice and water layers, a nomenclature is adopted where P represents a compressional wave in the ice shell, S a shear wave in the ice shell, and where C is an acoustic wave in the subsurface ocean that includes reflection from water–mantle interface. Following this convention, appropriate letters are added consecutively when an acoustic ray reflects from or transmits through a given environmental interface. A PS wave, for example, is a compressional wave that departs from the source, reflects as a shear wave at the ice–water interface and arrives at the receiver. A PCS wave is a compressional wave that transmits through the ice–water interface, reflects from the water–mantle interface, returns to the bottom of the ice shell, and transmits back into the ice as a shear wave. It should be noted that SP and PS waves arrive

at a receiver simultaneously since their ray paths are symmetric. Also, an S wave from a source to a receiver on the ice–vacuum surface is a Rayleigh wave.

Some labelled ray geometries are shown in Fig. 8. A ray path follows a straight line in an iso-speed medium. However, if the sound speed in the medium varies along the ray path, the ray must satisfy Snell’s law where reflection and transmission will occur at the boundary between iso-speed layers, and a continuous bending of a ray path, or refraction, will occur given a continuous sound speed gradient. For a horizontally stratified medium where sound speed varies only in the  $z$ -direction, the radius of curvature  $r_c$  of a refracting ray is

$$r_c = \frac{c_0}{\sin \theta_0} \left| \frac{dc}{dz} \right|^{-1}, \tag{18}$$

where  $\theta_0$  is the incident angle at some fixed depth as in Fig. 8 and  $c_0$  is the sound speed at the same depth. For the 20-km convective ice shell model, the minimum radius of curvature of a compressional wave in upper thermal boundary layer regime is 51 km, which is not perceptible in Fig. 7. Refracted propagation of sound is a common feature in terrestrial oceans. In mid-latitudes deep sound channels typically form due to thermal heating above and increasing pressure below. These enable sound waves to propagate for thousands of kilometers without ever interacting with the sea surface or bottom (Urlick, 1983). Without more evidence, however, it is difficult to speculate on what sound speed profiles may exist in a potential European ocean.

The travel time from a source to receiver depends on the ray path. Travel time differences between ray paths can be used to infer Europa’s interior structure. The range between a surface source event and a surface geophone can be obtained from direct P and S wave arrivals given the compressional and shear wave speeds in ice, which can be estimated with reasonable accuracy based on *a priori* information (see Appendix A). With the additional travel time measurement of a single ice–water reflection, such as PP, PS, or SS, the

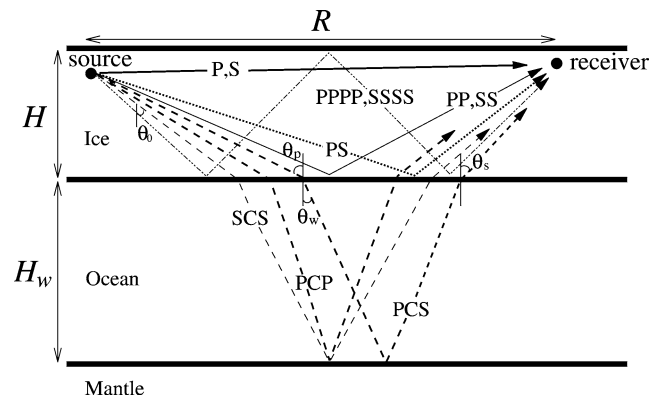


Fig. 8. Nomenclature of acoustic rays. PP, PS, SS waves are single reflections from the ice–water interface, and PPPP, SSSS waves are double reflections from the ice–water interface. PCP, PCS, and SCS waves are the reflections from the water–mantle interface. Sound speeds in ice layer and ocean layer are assumed constant in this figure.

thickness of the ice shell can be estimated. If more than one of these reflected paths are used, the sound speed in ice can also be experimentally estimated to improve upon the *a priori* information. Once the range of the source and the ice shell thickness are obtained, the depth of a subsurface ocean can be estimated by the reflections from the water–mantle interface, using any of the PCP, PCS, or SCS ray paths. The use of this kind of travel time analysis to infer Europa's interior structure will be discussed in more detail in Section 5.

#### 4.3. Synthetic seismograms for a Big Bang event

Here we study the amplitude and arrival-time structure of a Big Bang surface source event as measured by a triaxial geophone on Europa's surface for the four stratified models of Europa described in Section 2. First we consider the arrival time and amplitude structure as a function of range between the surface source and receiver by identifying the direct arrivals and reflections from various internal strata. Then we look in more detail at the type of amplitude and arrival time measurements that may be made at specific ranges. The analysis proceeds by solving the full-field seismo-acoustic wave equations of Eqs. (5) to (16) for a Big Bang source with a spectral peak in the 1–4-Hz range. The source is here modeled as a monopole at 50-m depth and the receiver as a triaxial geophone at 1-m depth beneath the ice–vacuum surface. The finite bandwidth of the radiation is computed by Fourier synthesis. The resulting simulations are referred to as synthetic seismograms when they show amplitude versus time, and time–range plots when they show amplitude versus time and range. All simulations in this section have been performed for  $h = 250$ -m cracks or equivalently an impactor of roughly 10-m radius. These figures can be scaled for various crack depths  $h$  and impactor volume injections  $s_0$  using Figs. 5 and 6, as explained in Appendix C (Eqs. (C.30) to (C.33)).

Time–range plots are shown in Figs. 9 and 10 for the convective ice shell model, and Figs. 11 and 12 for the rigid ice shell model. In each figure, two lines consistently depart without curvature from the origin. These are the direct P wave and Rayleigh wave arrivals in the ice. The Rayleigh wave has the highest amplitude since it propagates as a trapped wave on the ice–vacuum surface.

Arrivals due to multiply reflected paths from the ice–water interface and the water–mantle interface are also readily observed. The travel time differences between the multiple reflections are closely related to the thickness of the ice shell. In the thin ice shell model (Fig. 11), the spacing between the multiple reflections is not much greater than the duration of the source event. This leads to one group of closely spaced arrivals reflected from the ice–water interface and another closely spaced group from the water–mantle interface. As the thickness of the ice shell increases, these multiple reflections separate more in the time domain as can be seen in Figs. 9, 10, and 12.

Inspection of the various scenarios indicates that the overall pattern of arrivals and amplitudes is very sensitive to the structure of Europa's ice–water layer, in particular, the absolute thicknesses and depths of the ice shell and ocean, as expected from basic echo-sounding principles. The pattern, however, is not very sensitive to the differences in internal temperature of the rigid versus convecting ice models, as can be seen by comparing Figs. 9 and 12. Other techniques involving seismo-acoustic tomography may be better suited to estimating the temperature structure.

Detailed characteristics of the time series measured by a surface geophone can be better observed in synthetic seismograms. We present illustrative examples for the 20-km convective ice shell model. Figures 13 and 14 present a scenario where the seismometer is located at short range (2-km) from the source, while Figs. 15 and 16 present a longer range (50-km) scenario. In both scenarios, a sufficiently diverse set of prominent and well separated arrivals are found to enable the source range, as well as the thickness of Europa's ice shell and ocean layer to be determined by echo sounding.

For the case of a short source–receiver separation, as in Fig. 13, both the direct P and S waves arrive so near in time that they cannot be distinguished. The P wave is in fact overwhelmed by the S wave, which is effectively the Rayleigh wave due to the proximity of the source and receiver to the free surface. All subsequent arrivals can be easily distinguished from each other since they are well separated in time. The first arrivals are multiple reflections from the ice–water interface. For such a short source–receiver separation, waves returning from the water arrive at near normal incidence to the ice–water interface in the present geometry, and so lead to very weak SV transmission into the ice. This explains the relative abundance of prominent and well separated arrivals from the mantle in vertical velocity and the paucity of such arrivals in horizontal velocity at the geophone in Fig. 14.

For the case of a much longer source–receiver separation, as in Fig. 15, the direct P and S (again, the Rayleigh wave), as well as multiple reflections from ice–water and water–mantle interfaces are well separated in the time domain.

## 5. Inferring Europa's interior structure by travel time analysis

### 5.1. Simplified Europa model

In the previous section, we showed that the arrival time structure of seismo-acoustic waves is far more sensitive to ice shell thickness and ocean depth than to the temperature variations in the ice shell associated with the various rigid and convecting models examined. The seismo-acoustic parameters most important to the measured arrival-time structure, namely the thickness of the ice shell and the depth of a subsurface ocean, can then be estimated by matching measured travel times with those derived from a simplified

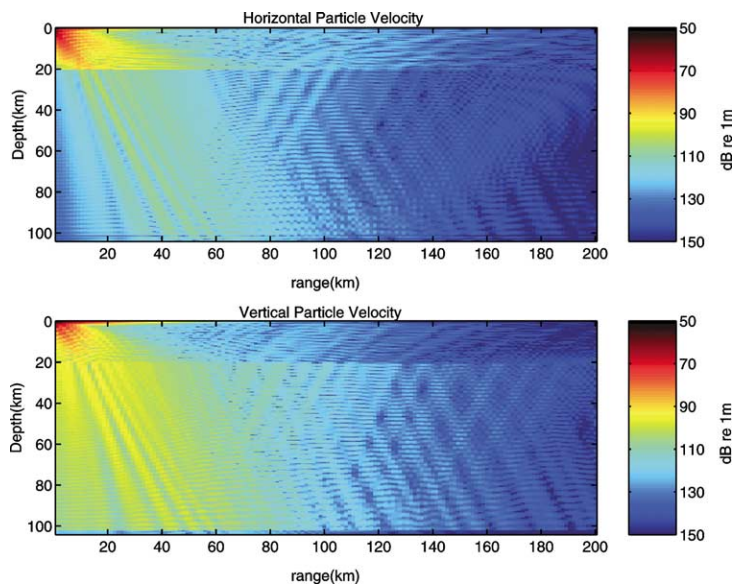


Fig. 7. Transmission loss plots of the horizontal particle velocity  $TL_{iH}$  (top) and vertical particle velocity  $TL_{iV}$  (bottom) as defined in Eq. (17), when the source is located 50-m below the surface.

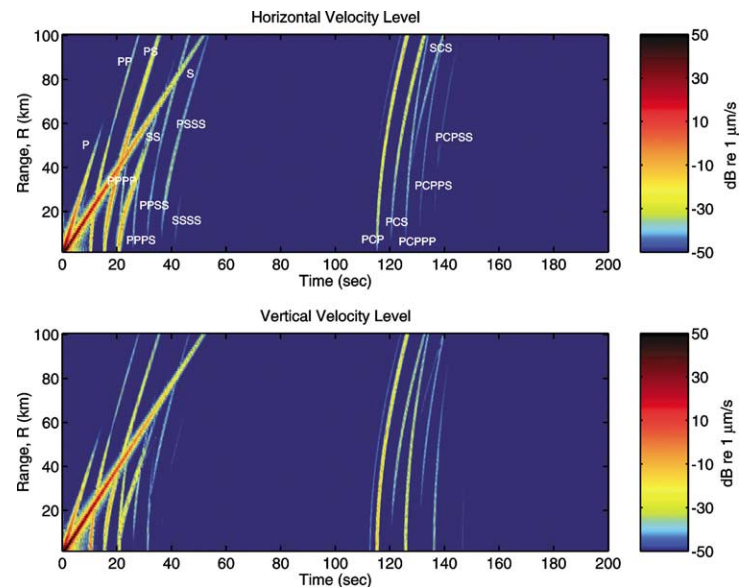


Fig. 9. Time-range plot for the 20-km convective ice shell model. Colors represent the horizontal velocity level  $L_{iH}$  (top) and vertical velocity level  $L_{iV}$  (bottom), as defined in Eqs. (C.18) and (C.19).

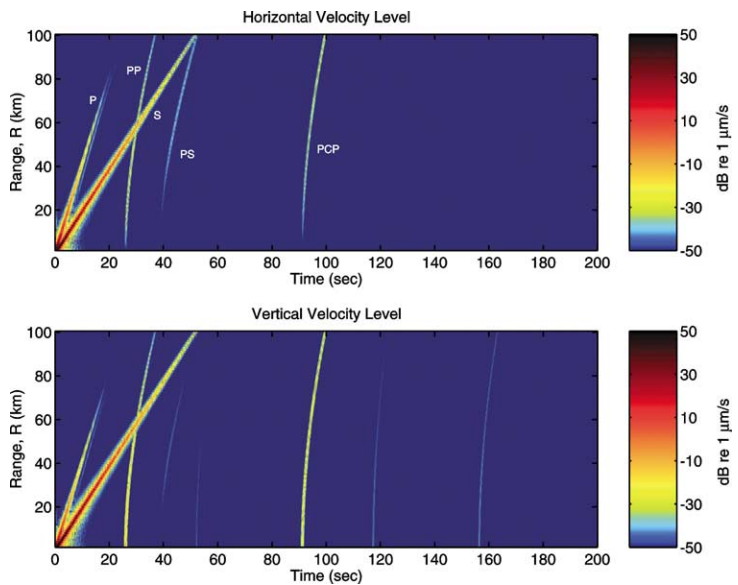


Fig. 10. Time-range plot for the 50-km convective ice shell model.

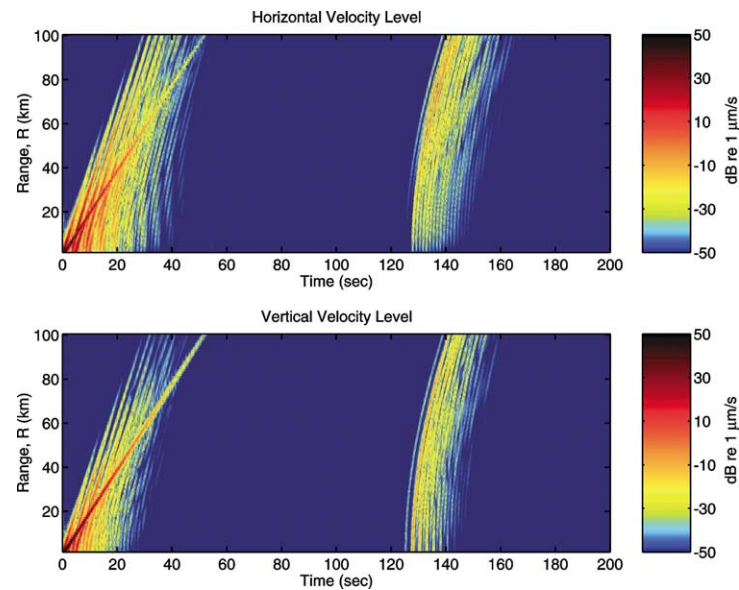


Fig. 11. Time-range plot for the 5-km rigid ice shell model.

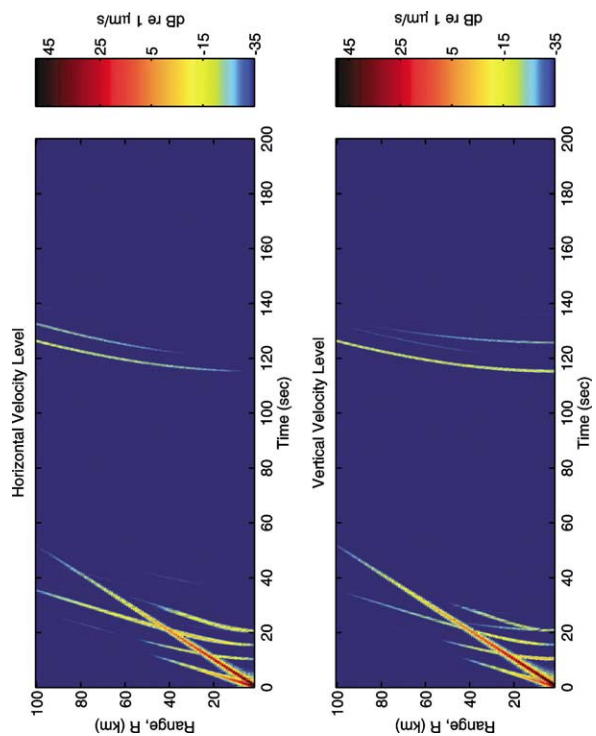


Fig. 20. Time-range plot for a Big Bang event that can stand above the reference ambient noise level of  $-35$  dB re  $1 \mu\text{m/s}$ .

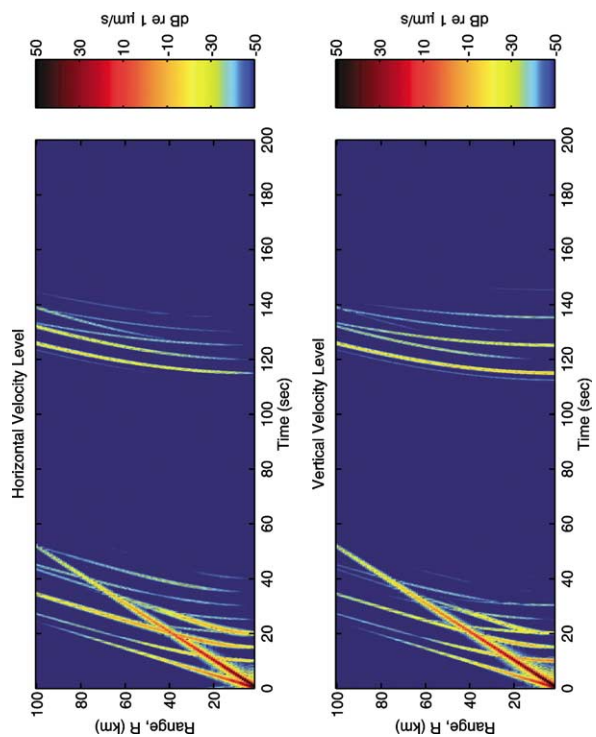


Fig. 12. Time-range plot for the 20-km rigid ice shell model.

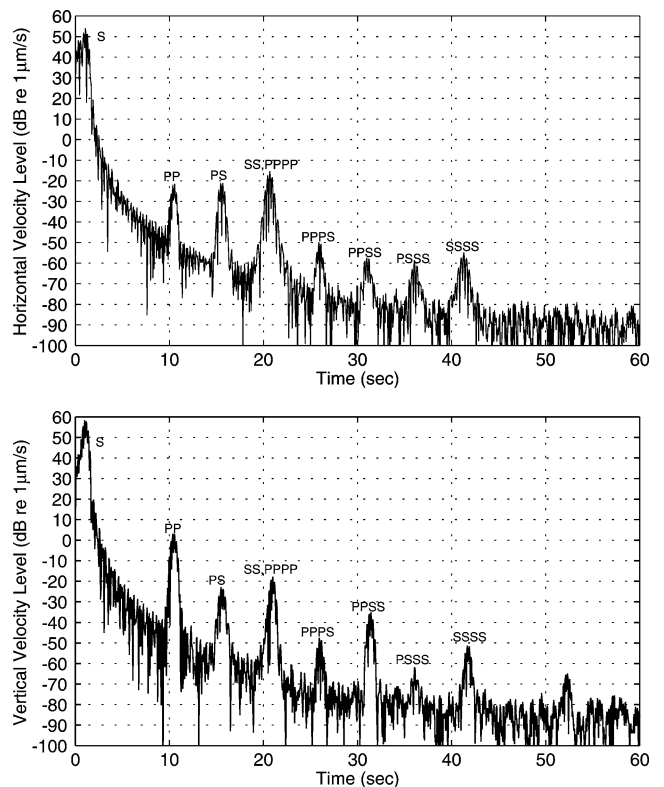


Fig. 13. Ice-water reflections at 2-km range for the 20-km convective ice shell model. The top figure shows the horizontal velocity level  $L_{ii}$  and the bottom figure shows the vertical velocity level  $L_{iv}$ , as defined in Eqs. (C.18) and (C.19). The regular spacing between the reflections can be directly related to the thickness of the ice shell. Direct P wave and Rayleigh wave arrivals are not well separated for this short range propagation.

European model. The simplified model drops parameters of Fig. 2 that do not have a first order effect in the arrival time structure. This leaves the six parameters shown in Fig. 17 at the top of the hierarchy. Dropped parameters, low in the hierarchy for the present echo-sounding technique, may be far more important in other inversion schemes.

The simplified Europa model employs an iso-speed ice shell. This is justified to first order for a number of reasons. Although Europa's ice layer may undergo a drastic change in temperature with depth, from roughly 100 to 273 K, the corresponding variations of  $c_p$  and  $c_s$  do not exceed 5%, as shown in Appendix A, except where the temperature reaches a few degrees of the melting point. This, however, occurs only over a small portion of the lower thermal boundary in the ice shell, as shown in Fig. 1. While the ice in this region undergoes changes in its molecular behavior, the change in sound speed is less than 10%. The overall error associated with the iso-speed assumption will then be less than 10%. In the simplified Europa model, we may further assume that  $\xi \equiv c_p/c_s = 2$ , which is a typical value for ice (Fig. A.1(c)).

## 5.2. General nondimensionalized travel time curves

Under the assumption of an iso-speed ice shell, following the simplified European model, the general surface source-

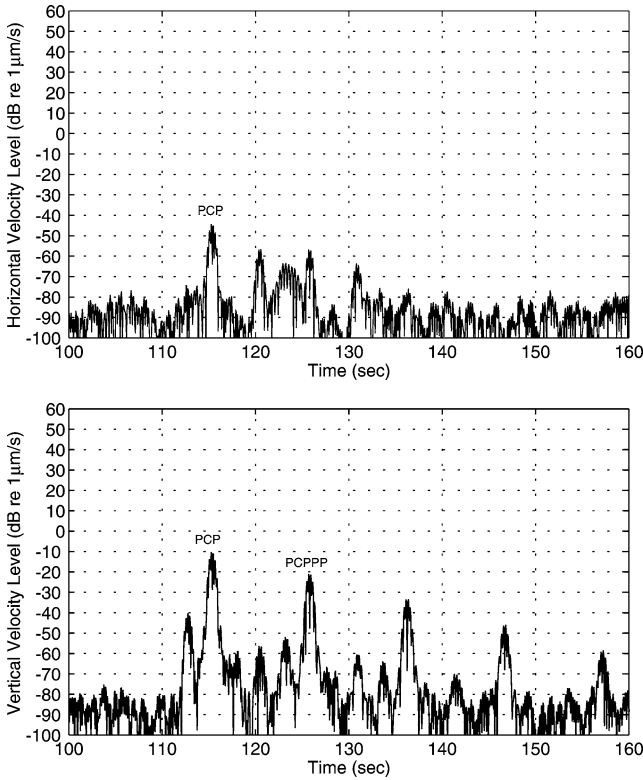


Fig. 14. Bottom reflections at 2-km range for the 20-km convective ice shell model. The bottom reflections for short range propagation are mostly compressional wave reflections, and are more prominent in the vertical particle velocity components. The weak precursor before the PCP reflection is the reflection from the sediment layer overlying the basalt halfspace.

to-receiver travel time of ice–water reflected paths can be determined as a function of two nondimensional parameters  $\xi$  and  $R/H$ , as shown in Appendix B. The travel time curves become functions of only one nondimensional parameter  $R/H$ , if we assume the typical value  $\xi = 2$ . Nondimensional travel time curves for the simplified Europa model are plotted in Fig. 18 where the travel time for paths including up to double reflections from the ice–water interface are shown. This figure can be used to analyze arrivals from ice–water reflections in Figs. 9 to 12.

Similarly, the general source-to-receiver travel time of paths involving water–mantle reflections can also be determined in terms of the additional nondimensional parameters  $\xi_w \equiv c_p/c_w$ , the ratio between the compressional wave speed in ice and water, and  $H_w/H$ , the ratio between the ocean depth and the ice shell thickness, assuming an isospeed water column. This is also shown in Appendix B. Nondimensional travel time curves for these paths are also plotted in Fig. 18, assuming  $H_w/H = 4$  and  $\xi_w = 4/1.5$ .

### 5.3. Estimating interior structure

The range between the source and receiver can be determined with a single triaxial geophone on Europa's surface without knowledge of the ice thickness by measuring the travel time difference between the direct P wave and the

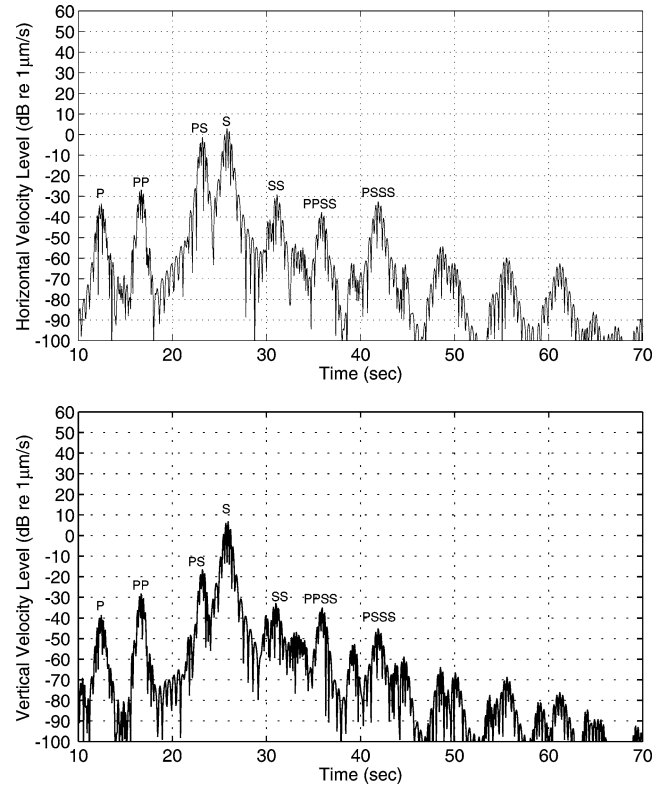


Fig. 15. Ice-water reflections at 50-km range for the 20-km convective ice shell model. Travel time differences between the direct P wave and the Rayleigh wave can be inverted for the range between the source and receiver, and multiple reflections from the ice–water interface can be inverted for the thickness of the ice shell.

Rayleigh wave. The Rayleigh wave can be easily identified by its high amplitude and retrograde particle motion where vertical and horizontal components are  $90^\circ$  out of phase.

To also estimate the thickness of the ice shell, at least one reflection from the ice–water interface must also be identified. The PP wave arrival can be readily identified since it arrives the soonest after the direct P wave except when  $R/H$  is less than one, as shown in Fig. 18. Even in this case, however, the PP wave can be easily identified, since, besides the direct P wave, the Rayleigh wave is the only wave that can arrive before it.

If, for example, we measure the travel time differences  $t_s - t_p \equiv \Delta_s$ , and  $t_{pp} - t_p \equiv \Delta_{pp}$ , where  $t_p$ ,  $t_s$ , and  $t_{pp}$  are the travel times of the direct P, the Rayleigh, and PP waves,

$$\Delta_s = \left( \frac{1}{0.93 c_s} - \frac{1}{c_p} \right) R = \frac{1}{c_p} \left( \frac{\xi}{0.93} - 1 \right) R, \quad (19)$$

$$\Delta_{pp} = \frac{1}{c_p} \left( \sqrt{4H^2 + R^2} - R \right), \quad (20)$$

and  $R/c_p$  and  $H/c_p$  are uniquely determined by,

$$\frac{R}{c_p} = \frac{\Delta_s}{\xi/0.93 - 1}, \quad (21)$$

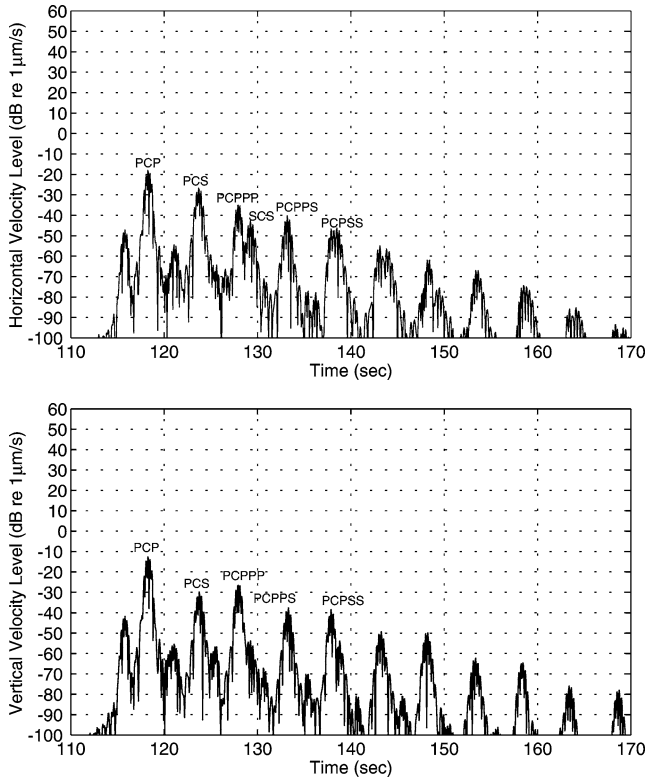


Fig. 16. Bottom reflections at 50-km range for the 20-km convective ice shell model. For long range propagation, bottom reflections are prominent in both the horizontal and vertical particle velocity components.

and

$$\frac{H}{c_p} = \frac{1}{2} \left[ \Delta_{pp} \left\{ \Delta_{pp} + \frac{2\Delta_s}{\xi/0.93 - 1} \right\} \right]^{1/2}. \quad (22)$$

This result shows that if the compressional wave speed in the ice is uncertain, but the ratio between the compressional and shear speed in ice is known, the error in the range and thickness estimates will be linearly related to the error in compressional wave speed. Based on the analysis presented in Appendix A, the sound speed in ice can be estimated to within roughly 10%. The range of the source and the thickness of the ice shell can then also be estimated within 10% of error given the travel times of the direct P, the Rayleigh, and PP waves. Estimates of  $R$ ,  $H$ ,  $c_p$ , and  $c_s$  can be refined by analyzing arrivals from other paths. Similarly, the ocean thickness  $H_w$  and average sound speed  $c_w$  can be determined by using Fig. 18 to analyze arrivals from paths reflecting from the water–mantle interface.

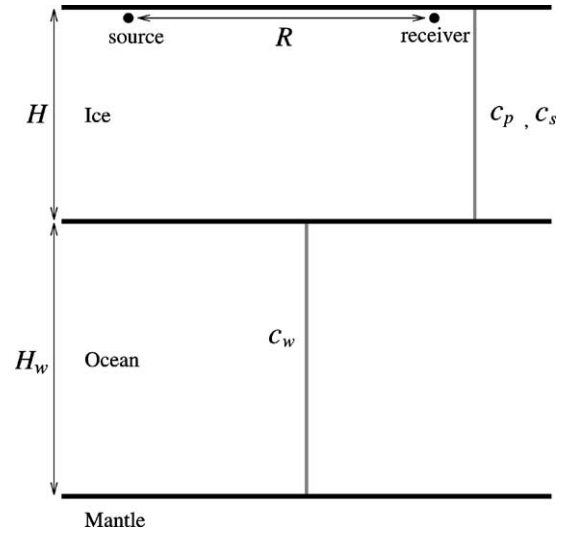


Fig. 17. Schematic diagram of the simplified Europa model used for the parameter inversion.  $R$  is the range between the source and seismometer. The ice shell and ocean are simplified into iso-speed layers.

Fig. 18. Nondimensionalized travel time curves for direct paths, ice–water reflections, and water–mantle reflections. It is assumed that  $H_w/H = 4$  and  $\xi_w = 4/1.5$  for bottom reflections. This figure can be directly compared to Figs. 9 and 12.

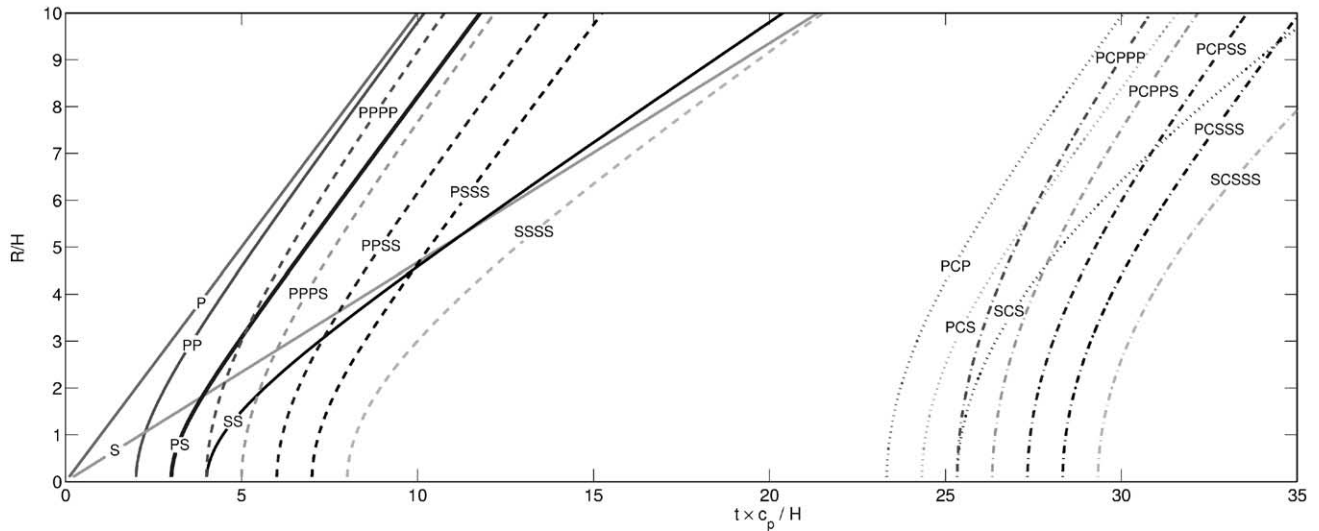


Fig. 18. Nondimensionalized travel time curves for direct paths, ice–water reflections, and water–mantle reflections. It is assumed that  $H_w/H = 4$  and  $\xi_w = 4/1.5$  for bottom reflections. This figure can be directly compared to Figs. 9 and 12.

## 6. European ambient noise

As noted in the introduction and in Section 3.1, there is a possibility that ice cracking events on Europa may occur so frequently in space and time that their accumulated effect may lead to difficulties for the proposed echo-sounding technique. Here we attempt to quantify the characteristics of a Big Bang event necessary for it to serve as a source of opportunity in echo sounding given an estimate of the accumulated noise received at a surface geophone. We do so by first developing a European noise model in terms of the spatial and temporal frequency and source spectra of the expected noise sources.

### 6.1. Estimation of ambient noise level

In order to calculate the ambient noise level, an ocean acoustic noise modeling technique (Kuperman and Ingenito, 1980) is adapted for Europa. The basic assumption is that the noise arises from an infinite sheet of monopole sources just below Europa's ice-vacuum boundary at depth  $z'$ . The sources are assumed to be spatially and temporally uncorrelated and to have the same expected source cross-spectral densities.

The mean-square horizontal and vertical particle velocities of the ambient noise measured by a geophone at depth  $z$  resulting from these uncorrelated sources are respectively

$$\langle |N_{\dot{u}}|^2 \rangle = \frac{\pi}{(\Delta T)(\Delta A)} \int_{-\infty}^{\infty} \langle |S(f)|^2 \rangle \times \int_0^{\infty} |g_{\dot{u}}(k_r, z, z')|^2 k_r dk_r df, \quad (23)$$

$$\langle |N_{\dot{w}}|^2 \rangle = \frac{2\pi}{(\Delta T)(\Delta A)} \int_{-\infty}^{\infty} \langle |S(f)|^2 \rangle \times \int_0^{\infty} |g_{\dot{w}}(k_r, z, z')|^2 k_r dk_r df, \quad (24)$$

where  $1/\Delta T$  and  $1/\Delta A$  are temporal and spatial densities of noise sources,  $\langle |S(f)|^2 \rangle$  is the expectation of the magnitude squared of source spectrum of a given source, and  $g_{\dot{u}}(k_r, z, z')$  and  $g_{\dot{w}}(k_r, z, z')$  are the integral representations of the horizontal and vertical particle velocities in the wavenumber domain, which are defined in terms of Hankel transform of Eqs. (5) and (6),

$$g_{\dot{u}, \dot{w}}(k_r, z, z') = \int_0^{\infty} G_{\dot{u}, \dot{w}}(r, z, z') J_0(k_r r) r dr. \quad (25)$$

The variance of the vertical particle velocity is the same as the scalar result given in Wilson and Makris (2003). The horizontal component is for one out of two horizontal directions

spanned by the geophone and so is smaller by a factor of 2. The ambient noise levels in decibels are defined by

$$NL_{\dot{u}} = 10 \log \frac{\langle |N_{\dot{u}}|^2 \rangle}{\dot{u}_{\text{ref}}^2} \text{ dB re } \dot{u}_{\text{ref}}, \quad (26)$$

$$NL_{\dot{w}} = 10 \log \frac{\langle |N_{\dot{w}}|^2 \rangle}{\dot{w}_{\text{ref}}^2} \text{ dB re } \dot{w}_{\text{ref}}, \quad (27)$$

where  $\dot{u}_{\text{ref}} = \dot{w}_{\text{ref}} = 1 \mu\text{m/s}$ .

Equations (23) and (24) are used to compute the general ambient noise levels measured by a geophone at 1-m below the ice-vacuum interface for the 20-km convective shell model as a function of temporal and spatial source density. The results are shown in Fig. 19 for noise sources at  $z' = 50\text{-m}$  depth in the 1–4-Hz band, the same depth and band used for the Big Bang synthetic seismograms of Section 3. This noise table is for  $h = 50\text{-m}$  ambient cracks, but can be scaled for other crack depths  $h$  by following the procedures described in Appendix C.

The ambient noise levels of Fig. 19 can be compared directly with the signal levels of 250-m cracks for the 20-km convective shell model (Figs. 9, 13, 14, 15, and 16). The noise levels can even be compared with the signal levels in Figs. 10, 11, and 12 because ambient noise level does not vary significantly as a function of ice shell thickness, since it is dominated by the Rayleigh wave, which is trapped on the ice-vacuum interface and so is relatively insensitive to the ice shell thickness  $H$  when its wavelength is small compared to  $H$ .

Such comparisons still require knowledge of the spatial and temporal densities of the noise sources. These can be estimated for diurnal tidally driven tensile cracks by noting that a cycloidal feature will extend at a speed of roughly 3.5 km/hr, following the location of maximum tensile stress

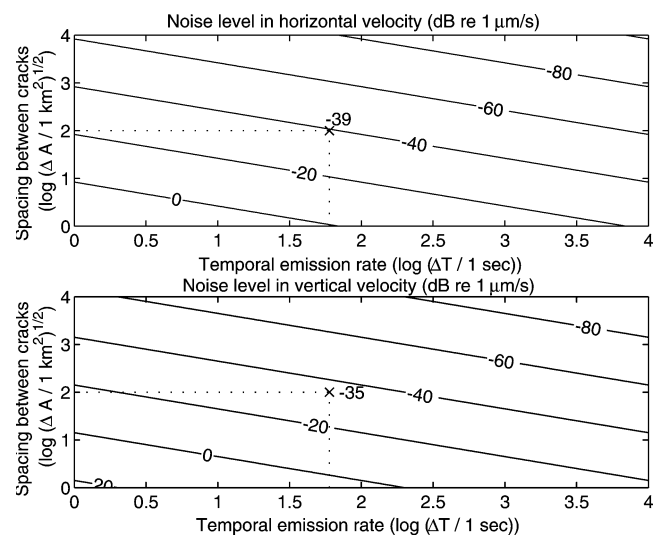


Fig. 19. Ambient noise levels in the horizontal velocity  $NL_{\dot{u}}$  and vertical velocity  $NL_{\dot{w}}$ , as defined in Eqs. (23) and (24), for the 20-km convective ice shell model as a function of spatial densities and temporal emission rates of the surface cracks. The reference ambient noise levels assuming  $\Delta T = 60\text{ s}$  and  $\Delta A = 100\text{ km}^2$  are marked in the figure.

(Hoppa et al., 1999). The propagation speed of a tensile crack, however, is the much larger  $v \simeq 0.9c_s$ , as noted in Section 3.1. The cycloidal features then are apparently comprised by a sequence of discrete and temporally disjoint cracking events. If we assume that each tidally driven crack, of nominal depth  $h = 50$ -m extends for a minimum length of  $h = 50$ -m, as discussed in Section 3.1, we arrive at a rate of roughly 1 tensile crack per minute along a given cycloidal feature. A consistent estimate of the spatial separation between cracking events would be the roughly 100-km scale of a cycloidal feature (Hoppa et al., 1999). As can be observed in Fig. 19, the ambient noise level reaches  $-35$  dB re  $1 \mu\text{m/s}$  for 100-km crack spacing and 1 discrete emission per minute.

If the source of opportunity and ambient noise sources have the same depth of  $h = 50$ -m, the expected energy of each noise source equals that of the signal. In this case, the amplitudes of the time-range plots and synthetic seismograms in Section 4.3 should be decreased by 56-dB, as can be determined from Eqs. (C.30) and (C.31) of Appendix C. Comparison with the time-range plots and synthetic seismograms of Section 4.3, after subtracting 56-dB to go from an  $h = 250$ -m to an  $h = 50$ -m deep crack, shows that the reflections from the ice–water and water–mantle interfaces will be buried by the ambient noise for this scenario. The situation changes if the source of opportunity is far more energetic than an expected noise event, as is the case for a Big Bang source event.

## 6.2. Estimation of signal to noise ratio

It was shown in Section 3.1 that the peak of the energy spectral density for a surface crack is proportional to  $h^6$ , while both the bandwidth and frequency of the spectral peak are inversely proportional to the crack depth  $h$ . Smaller cracks will then not only radiate less energy, they will also spread this energy over a broader and higher frequency spectrum. Larger cracks, on the other hand, will radiate more energy over smaller bandwidths at lower frequencies, as shown in Fig. 4. This would make it advisable to low-pass filter geophone time series data to the band of a Big Bang source of opportunity, if this source was due to a much deeper and less frequent cracking event than those comprising the expected noise. If the Big Bang is 5 times deeper than the ambient cracks, for example, the radiated energy within the bandwidth of the Big Bang will be approximately 56-dB greater than that radiated by an ambient crack. This will in turn increase the signal-to-noise ratio of the time series by 56-dB. In this case, it will be possible to robustly detect multiple Big Bang reflections from the ice–water interface and water–mantle interface above the noise for nominal 50-m deep noise cracks of 100-km spacing and 1 per minute rate, as is illustrated in Fig. 20 for a 250-m deep Big Bang crack.

According to Nur (1982), unfractured ice subject to a fixed tensile stress will develop a distribution of surface frac-

tures that occur at a rate inversely proportional to the maximum depth of the crack  $h$ . Larger cracks will be less frequent and so less likely radiate seismo-acoustic waves that overlap. Larger cracks will also release stress over larger areas and so prevent other cracks from developing nearby.

Small impacts are another potential source of Big Bang events that usually have much higher energy spectral levels than surface cracks, as can be seen by comparing Figs. 5 and 6. Given the impact rate mentioned in Section 3.2, the probability of at least one impactor within 100 km of the seismometer is 0.1 to 10% assuming a 4 month operational period. While such an impact is not highly likely, the signal-to-noise ratio would be large and the reflections could be easily resolved. Smaller impacts may be much more frequent and still energetic enough to serve as Big Bang events, but their rates are difficult to resolve with current observational methods.

Our signal-to-noise-ratio analysis is based on the worst-case scenario of maximum diurnal stress, where all surface cracks are assumed to actively radiate seismo-acoustic waves once every minute. Cracking will become less frequent after Europa passes the perigee. The ambient noise level will then decrease, enabling echo-sounding with a surface crack of shallower depth  $h$ . Since impactors are totally independent of surface cracking noise, they may strike Europa at low-tide when surface cracks are dormant, achieving the maximum signal to noise ratio.

## 7. Inferring interior properties of Europa with love and Rayleigh waves

Love waves are effectively propagating SH modes trapped by the boundaries of an elastic waveguide, while Rayleigh waves are interface waves that travel along an elastic surface that involve both compressional and SV wave potentials. The theory of these waves in horizontally stratified media is well developed (see, e.g., Brekhovskikh, 1980; Miklowitz, 1978). Here we discuss the possibility of using the frequency dependent characteristics of these waves to infer interior properties of Europa.

### 7.1. Dispersion of the Love wave

If an elastic medium is surrounded by a vacuum or fluid media that does not support shear, as in the case of an ice sheet floating on an ocean, the Love wave will propagate like a free wave in a plate.

Considering the geometry in Fig. 21, it can be shown that SH waves will propagate as discrete normal modes with the group velocity of each mode given as

$$U_l = c_s \left[ 1 - \left( \frac{\pi l}{\kappa H} \right)^2 \right]^{1/2}, \quad l = 0, 1, \dots, l_{\max}. \quad (28)$$

The maximum number of normal modes for a given frequency is

$$l_{\max} = \text{integer part of } \left( \frac{\kappa H}{\pi} \right), \quad (29)$$

with the cut-off frequency of each mode is given as

$$f_{c,l} = \frac{c_s l}{2H}. \quad (30)$$

It is important to note that there is a zeroth-order mode that is non-dispersive, insensitive to the thickness, and has no cut-off frequency, which can be obtained by setting  $l = 0$  in Eqs. (28) and (30). This characteristic of zeroth-order mode is also shown in Fig. 22.

This derivation shows that Love waves in a free or fluid loaded plate have group velocities that are inversely proportional to frequency so that the lower frequency components propagate slower than the higher ones. This dispersive characteristic is shown for the group velocity of the 1st mode for various ice shell thicknesses in Fig. 22.

If the ice shell overlies another elastic medium with faster shear wave speed such as Europa's mantle, however, at the low frequency end the dispersion relationship will be reversed with the lower frequency components arriving faster than the higher frequency components. This is a common effect also observed in ocean acoustic waveguides (Pekeris, 1948; Frisk, 1994). In this case, it can be shown that the

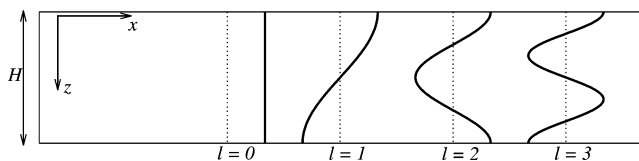


Fig. 21. Love wave geometry and mode shapes for an elastic plate surrounded by fluid media.

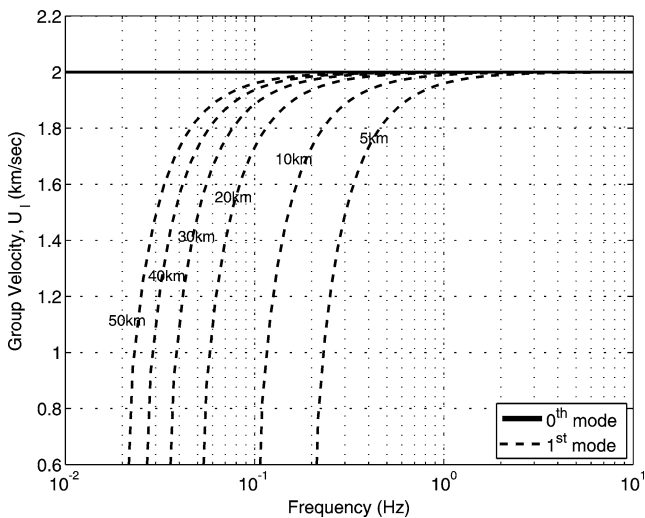


Fig. 22. Love wave dispersion curves for various ice shell thicknesses assuming an iso-speed ice shell with a shear wave speed  $c_s = 2$  km/s, overlying a subsurface ocean. The 0th order mode has a constant group velocity that is independent of the ice shell thickness.

group velocity and cut-off frequency of each mode is given by

$$U_l = \kappa_{x,l} \left[ \frac{H \sqrt{\kappa_{x,l}^2 - \kappa_b^2}}{\cos^2(H \sqrt{\kappa^2 - \kappa_{x,l}^2})} + \frac{\mu_b}{\mu} \left\{ 1 + \frac{\kappa_{x,l}^2 - \kappa_b^2}{\sqrt{\kappa^2 - \kappa_{x,l}^2}} \right\} \right] \times \left( \frac{\kappa}{c_s} \frac{H \sqrt{\kappa_{x,l}^2 - \kappa_b^2}}{\cos^2(H \sqrt{\kappa^2 - \kappa_{x,l}^2})} + \frac{\mu_b}{\mu} \left[ \frac{\kappa_b}{c_{sb}} + \frac{\kappa}{c_s} \frac{\kappa_{x,l}^2 - \kappa_b^2}{\sqrt{\kappa^2 - \kappa_{x,l}^2}} \right] \right)^{-1}, \quad (31)$$

$$f_{c,l} = \frac{l}{2H} \frac{c_s c_{sb}}{\sqrt{c_{sb}^2 - c_s^2}}, \quad (32)$$

where  $\kappa_{x,l}$  is the wavenumber of  $l$ th mode in  $x$  direction, and  $\mu_b, c_{sb}, \kappa_b$  are the shear modulus, shear wave speed, and shear wavenumber in the elastic medium underlying the ice shell, respectively. The mode shapes and dispersion curves for various ice shell thicknesses assuming an ice shell overlying basalt halfspace are shown in Figs. 23 and 24, respectively.

Kovach and Chyba (2001) have argued that it may be possible to verify the existence of a subsurface ocean on Europa by finding a way to measure the presence or absence of this reversal. Since the Love wave is trapped within the ice shell,

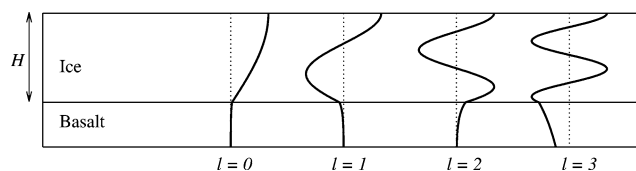


Fig. 23. Love wave geometry and mode shapes assuming an ice shell overlying basalt halfspace.

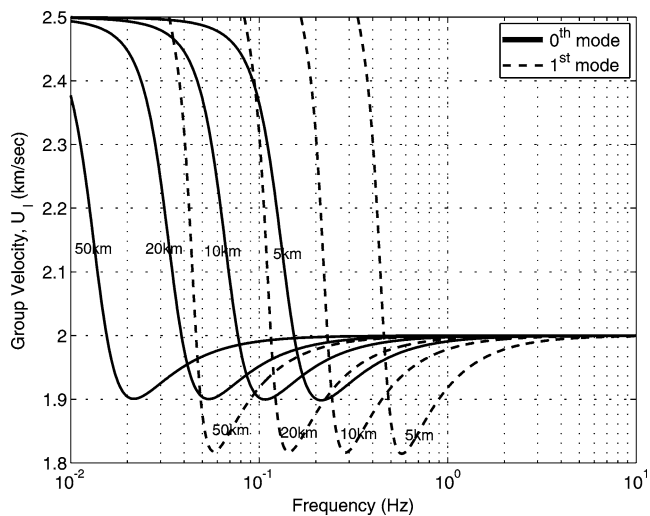


Fig. 24. Love wave dispersion curves for the 0th and 1st order modes in the case where ice shell is overlying a basalt halfspace.

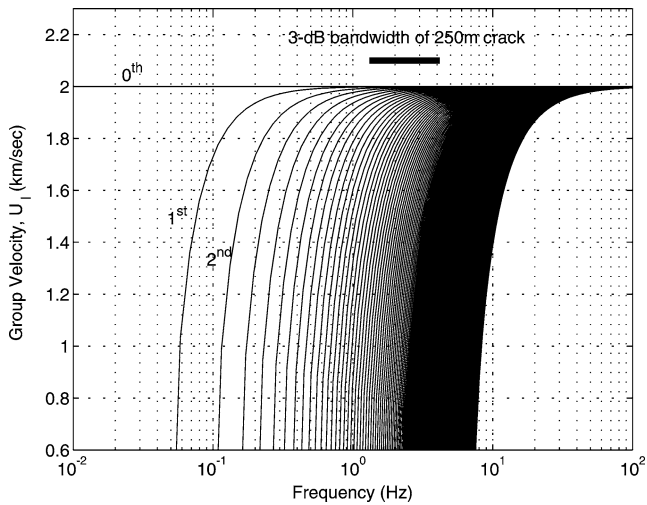


Fig. 25. Love wave dispersion curve for the 20-km fluid-loaded iso-speed ice shell up to the 144th mode. The mode number runs from left to right. For reference, the 3-dB bandwidth of a 250-m deep crack is shown as a thick horizontal line.

it cannot be used to determine the depth of a potential ocean layer below. Kovach and Chyba (2001) have also suggested that it may be possible to determine the thickness of the ice layer by measuring the frequency dependence or dispersion in the group velocity of the first Love wave mode.

Since Love waves are modal decompositions of the SH wave, they will likely require source-receiver ranges greatly in excess of the ice sheet thickness to be observed. Group velocity analysis, however, requires the source range, which can be estimated by measuring the direct P wave arrival for sufficiently energetic sources or multiple reflections from the ice-water interface. Use of the latter, however, would require the ice thickness be determined by echo-sounding, which defeats much of the purpose in Love wave dispersion analysis.

Since the Love wave has a zeroth order mode that is non-dispersive if an ocean is present and has no cut-off, a potentially significant component of any Love wave arrival may never exhibit the sought after frequency dependence or cut-off. Additionally, many modes higher than the 1st can be easily excited by the broadband surface sources described in Section 3.1 as shown in Fig. 25 for the fluid-loaded scenario. Different order modes from different frequencies must then somehow be separated to avoid ambiguities in the estimation of the group-speed frequency dependence of a given mode. Such separation will be difficult to obtain with a single sensor and an uncontrolled source.

A measurement of reduced Love wave levels in the low frequency regimes near modal cut-offs could then easily be due to the lower source energy spectra expected in these regimes from the analysis of Section 3.1 rather than modal cut-off effects. Comparisons with P wave and SV wave spectra from the same source event could help to reduce this ambiguity, but would not necessarily resolve it even below the cut-off frequency of the 1st mode due to the existence of the 0th order Love wave mode that is non-dispersive in the

fluid-loaded scenario and has no cut-off. Some of these issues may be resolvable for very distant sources given well separated arrivals for the different Love wave modes.

## 7.2. Estimating the upper ice shell temperature gradient by Rayleigh wave dispersion

It may be possible to estimate the temperature gradient in the upper thermal boundary layer of the ice shell by measuring dispersion of the Rayleigh wave. As noted earlier, the Rayleigh wave is a special kind of surface wave that propagates as a trapped wave on the boundary between the vacuum and the elastic medium. Since its propagation speed is slower than the shear speed in ice, it cannot propagate downward but rather decays exponentially with depth as an “evanescent wave” in the ice. This decay is often referred to as an evanescent tail that reaches down into the elastic medium. Since the length of evanescent tail is dependent on frequency, different frequency components of the Rayleigh wave will probe different depths. The Rayleigh waves at different frequencies, probing different depths, will then disperse in time if the shear speed of the ice changes with depth. A strong sound speed gradient in the ice shell, as in the convective ice shell model, will then force Rayleigh waves to disperse over time. Measurement of this dispersion may reveal the internal sound speed profile of the ice shell, from which the temperature profile may be inferred. Contrary to the problems encountered with Love waves, a broader source spectrum gives better resolution in measuring the dispersion of Rayleigh waves since the Rayleigh wave is a single wave type rather than a set of propagating modes.

The actual measurement of Rayleigh wave dispersion has some similar practical constraints as those encountered for the Love wave measurement. The range from source to receiver and original energy spectrum of the source must be known. These, however, may be reasonably estimated by measuring the direct P wave arrival time and energy spectrum, as is necessary in echo sounding. To sample deep into the ice shell, very long wavelengths and consequently very low frequency components must be strongly excited. These require large cracking events. Frequency components less than 0.5 Hz, for example, would need to be strongly excited for the 20-km ice shell model. Also, since the sound speed in ice does not change drastically with temperature, as shown in Appendix A, long-range propagation, well in excess of 100 km, is necessary to clearly resolve the dispersion. For example, a 0.2-km/s variation in the shear wave speed across the upper thermal boundary layer in the convective ice shell model will lead to an approximately 5-s travel time difference between the high and low frequency components at 300 km. So as in both the echo sounding and Love wave techniques, extremely energetic events are required, and as in the Love wave technique the source of opportunity must be very distant for the Rayleigh wave dispersion technique to be feasible.

## 8. Summary and conclusions

A method to probe the interior structure of Europa by echo-sounding with natural sources of opportunity is presented. To evaluate its feasibility, estimates are made of (1) the frequency of occurrence and energy spectra expected of typical European seismo-acoustic sources, (2) the travel time and amplitude structure of arrivals from these sources at a distant receiver after propagation through Europa's ice and potential water layers, and (3) ambient noise on Europa.

We find that a single passive triaxial geophone planted on Europa's surface should make it possible to estimate the thickness of Europa's ice shell as well as the depth of a potential subsurface ocean by exploiting natural ice cracking events and impactors as seismo-acoustic sources of opportunity. These natural sources are expected to radiate low frequency seismo-acoustic waves that are well suited for efficient propagation deep into the interior of Europa. Our analysis shows that "Big Bang" source events are likely to occur within the period of a landing mission that have returns from the bases of the ice and ocean layers of sufficient magnitude to stand above the accumulated ambient noise of less energetic but more frequent surficial cracking events.

## Appendix A. Acoustic properties of ice

Europa has an average surface temperature of roughly 100 K, a value much lower than is found in natural terrestrial ice. To estimate the seismo-acoustic properties of European ice, we resort to theory, extrapolation from laboratory data obtained at extreme temperatures, and data from Arctic field experiments. While this approach should provide reasonable estimates, within roughly 10%, further investigation of the seismo-acoustic properties of ice at extremely low temperature and high pressure would be beneficial.

### A.1. Seismo-acoustic of wave speed

Several *in situ* and laboratory measurements of the dependence of compressional and shear wave speeds on temperature have been made in ice.

Proctor (1966) measured wave speeds for temperatures between 60 and 100 K in pure ice, and suggested equations for the elastic compliance constants. Given the elastic compliance constants, the average sound speed in hexagonal systems such as ice can be calculated by the method of Anderson (1963). The results are shown in Fig. A.1 along with several *in situ* measurements (Robin, 1953; Joset and Holtzschler, 1953; McCammon and McDaniel, 1985) assuming the density of ice  $\rho_i = 930 \text{ kg/m}^3$ . In Fig. A.1, the Voigt and Reuss approximations represent the upper and lower bounds of the elastic constants, while the Hill approximation is the arithmetic mean of these two. Anderson (1963) suggested the Hill approximation as an average sound speed for hexagonal systems. Figure A.1, however, shows that *in*

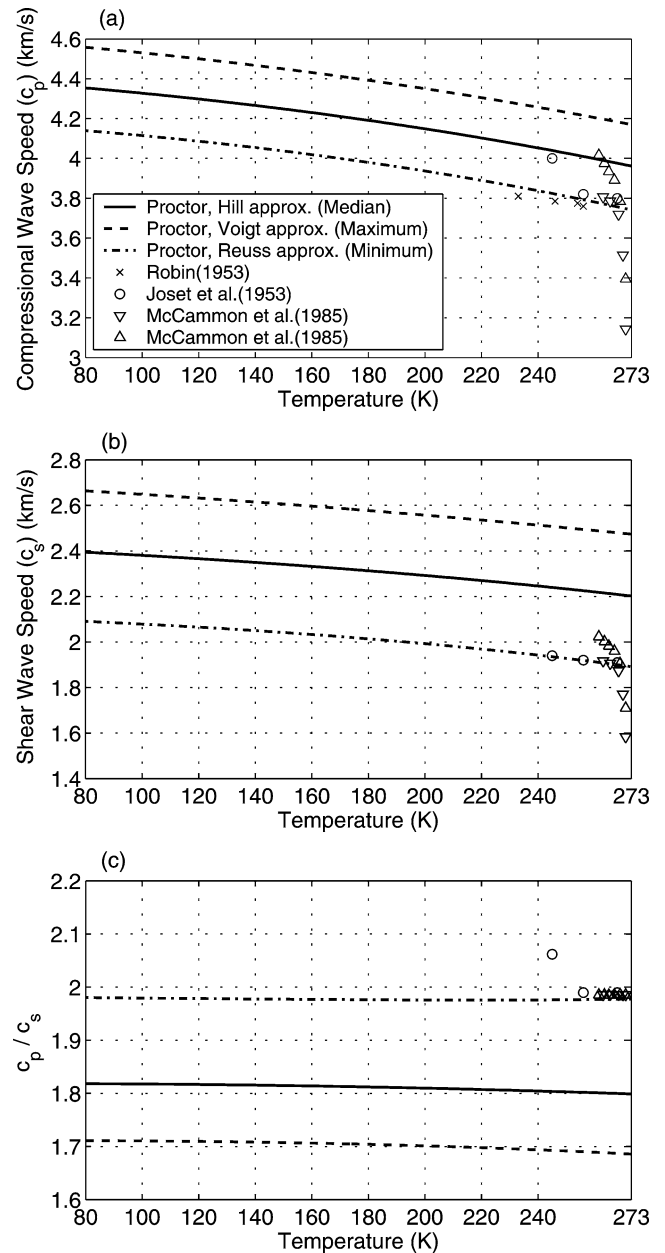


Fig. A.1. Compressional, shear wave speeds and the ratio as a function of temperature.

*situ* measurements agree better with the Reuss approximation. It appears that the porosity in sea ice induced by air bubbles or brine cells significantly lowers the elastic constants of sea ice with respect to pure crystalline ice. Mellor (1983) also pointed out that Young's modulus in ice varies significantly with porosity. Noting that the magnetic signature of Europa suggests a salty ocean with salinity comparable to that of the Earth (Khurana et al., 1998), we conclude that the Reuss approximation using Proctor's elastic compliance constant equations will best estimate the sound speed profiles in the Europa's ice shell, and employ this approximation to construct the wave speed profiles in Fig. 1.

There are several measurements suggesting a strong change in compressional and shear wave speed at temperatures near the melting point of ice (Hunkins, 1960; Lotze, 1957). This effect can be also observed in Fig. A.1. Since the regime near the melting point in Europa's ice shell occupies only a small portion of the total ice shell (Fig. 1), we ignore this effect in the compressional and shear speed profiles, since the error introduced in echo sounding will likely be negligible.

It is significant that the total change in speed, for compressional and shear waves in ice, over temperature is small compared to the speed at any given temperature. The compressional wave speed, for example, ranges from 3.7 to 4.1 km/s over Europa's ice shell temperature range of 100 to 270 K, exhibiting only a 5% variation about the mean compressional wave speed of 3.9 km/s. Similarly mild variation is observed in the shear wave speed. The ratio of the compressional to shear wave speed  $\xi$ , moreover, is a very weak function of temperature, and has a typical value of 2 in both the Reuss approximation and the *in situ* measurement data, as shown in Fig. A.1(c).

The dependence of compressional and shear wave speed with pressure in ice has been primarily determined by laboratory experiments with pure polycrystalline ice (Shaw, 1986; Gagnon et al., 1988). These experiments show only 1% change of wave speed in the pressure range between 0 bar to 1 kbar, the expected pressure range in the European ice shell. We expect that pressure variation will have a negligible effect on compressional and shear wave propagation speeds in the European ice shell.

The elastic properties such as Young's modulus  $E$  and Poisson's ratio  $\nu$  can be obtained from the wave speeds assuming an isotropic medium,

$$E = \rho_i c_s^2 \frac{3\xi^2 - 4}{\xi^2 - 1}, \quad (\text{A.1})$$

$$\nu = \frac{1}{2} \frac{\xi^2 - 2}{\xi^2 - 1}. \quad (\text{A.2})$$

The wave speed curves in Fig. A.1 suggest that the Young's modulus of ice can vary from 9 to 11 GPa in the temperature regime of Europa, and Poisson's ratio  $\nu = 0.333$ . In this paper, we used  $E = 10$  GPa as an average value over the ice shell.

## Appendix B. Nondimensionalization of the travel time curves

Assuming an iso-speed ice shell, the time-range plots in Section 4.3 can be nondimensionalized by dimensionless parameters  $t c_p/H$ ,  $R/H$ , and  $\xi$ . Furthermore, we can assume that  $\xi = 2$ , as mentioned in Appendix A. In this case, the nondimensionalized travel times  $t c_p/H$  of all the direct waves and ice–water reflections can be expressed using only one parameter  $R/H$  to generate the nondimensional travel time curve in Fig. 18.

Nondimensionalization of water–mantle reflections assuming iso-speed ocean can also be achieved by introducing additional nondimensional parameters  $H_w/H$  and  $c_p/c_w$ .

### B.1. Nondimensionalization of direct paths

The travel times of the direct P wave and the Rayleigh wave are

$$t_p = \frac{R}{c_p}, \quad (\text{B.1})$$

$$t_s = \frac{R}{0.93c_s}. \quad (\text{B.2})$$

The propagation speed of Rayleigh wave is  $0.93c_s$  when  $\xi = 2$ .

These equations can be nondimensionalized by multiplying  $c_p/H$  to both sides of Eqs. (B.1) and (B.2):

$$\frac{t_p c_p}{H} = \frac{R}{H}, \quad (\text{B.3})$$

$$\frac{t_s c_p}{H} = \frac{\xi}{0.93} \frac{R}{H}. \quad (\text{B.4})$$

### B.2. Nondimensionalization of multiple reflections from the environmental interfaces

Let  $t_{\text{ray}}$  to be a travel time of a specific acoustic ray following the ray nomenclature in Section 4.2, and let

$n_p$  = number of occurrences of P in ray nomenclature,

$n_s$  = number of occurrences of S in ray nomenclature,

$n_c$  = number of occurrences of C in ray nomenclature.

For example, for PSSCP ray path,  $n_p = 2$ ,  $n_s = 2$ ,  $n_c = 1$ . Then it can be shown that the nondimensionalized travel time of each ray is given by

$$\frac{t_{\text{ray}} c_p}{H} = \frac{n_p}{\cos \theta_p} + \frac{n_s}{\cos \theta_s} \xi + \frac{2n_c}{\cos \theta_w} \frac{H_w}{H} \xi_w, \quad (\text{B.5})$$

where  $\theta_p$ ,  $\theta_s$ , and  $\theta_w$  satisfy

$$n_p \tan \theta_p + n_s \tan \theta_s + 2n_c \frac{H_w}{H} \tan \theta_w = \frac{R}{H}, \quad (\text{B.6})$$

$$\sin \theta_p = \xi \sin \theta_s = \xi_w \sin \theta_w. \quad (\text{B.7})$$

Equation (B.6) is derived from the source, receiver, and waveguide geometry. An acoustic ray must satisfy Snell's law along the ray path as given in Eq. (B.7). The terms on the right-hand side of Eq. (B.5) represents the travel time of the compressional wave and shear wave in the ice shell, and the travel time of the acoustic wave in the ocean, respectively.

## Appendix C. Radiated energy spectra, transmission loss, and scaling laws

Here we first derive the equations that relate the radiated energy level, source level, and particle velocity level from

a monopole or pure volume injection source in an infinite homogeneous medium and then generalize these results to a waveguide.

Assuming an omnidirectional volume injection source at the center of a spherical coordinate system  $(r_s, \theta, \varphi)$ , the inhomogeneous wave equation in the time domain is

$$\nabla^2 \phi(r_s, t) - \frac{1}{c_p^2} \frac{\partial^2 \phi(r_s, t)}{\partial t^2} = -s(t) \delta(\mathbf{r}_s), \quad (\text{C.1})$$

where  $\delta(\mathbf{r}_s)$  is 3D delta function, and  $s(t)$  is volume injection amplitude in the time domain. The solution to Eq. (C.1) in an infinite homogeneous medium with no boundaries is that obtained by d'Alembert

$$\phi(r_s, t) = \frac{s(t - r_s/c_p)}{4\pi r_s}, \quad (\text{C.2})$$

and the radial displacement component is

$$\begin{aligned} u_{r_s}(r_s, t) &= \frac{\partial \phi(r_s, t)}{\partial r_s} \\ &= -\frac{1}{4\pi} \left[ \frac{s(t - r_s/c_p)}{r_s^2} + \frac{\dot{s}(t - r_s/c_p)}{r_s c_p} \right]. \end{aligned} \quad (\text{C.3})$$

The first term in the bracket is a near field term proportional to  $1/r_s^2$ , and the second term is a radiating displacement component. By considering the radiating component only, the radial particle velocity is

$$\dot{u}_{r_s}(r_s, t) = -\frac{\ddot{s}(t - r_s/c_p)}{4\pi r_s c_p}. \quad (\text{C.4})$$

Given the particle velocity, the total radiated energy  $E_T$  from the source is the integral of the energy flux over an area enclosing the source and over time,

$$\begin{aligned} E_T &= \rho c_p \int_{-\infty}^{\infty} \int_0^{2\pi} \int_0^{\pi} |\dot{u}_{r_s}(r_s, t)|^2 r_s^2 \sin \theta \, d\theta \, d\varphi \, dt \\ &= 4\pi r_s^2 \rho c_p \int_{-\infty}^{\infty} |\dot{u}_{r_s}(r_s, t)|^2 \, dt. \end{aligned} \quad (\text{C.5})$$

The radiated energy spectrum is defined using Parseval's identity,

$$\epsilon(f) = 8\pi r_s^2 \rho c_p |\dot{u}_{r_s}(r_s, f)|^2. \quad (\text{C.6})$$

From Eq. (C.4), the radial particle velocity in the frequency domain is

$$\dot{u}_{r_s}(r_s, f) = \frac{(2\pi f)^2}{4\pi r_s c_p} S(f) e^{-i2\pi f r_s/c_p}, \quad (\text{C.7})$$

where the source spectrum  $S(f)$  is the Fourier transform of the source volume  $s(t)$ . From Eqs. (C.6) and (C.7),

$$\epsilon(f) = \frac{8\pi^3 \rho f^4}{c_p} |S(f)|^2. \quad (\text{C.8})$$

Taking the log of both sides of Eq. (C.8),

$$\begin{aligned} 20 \log \frac{|S(f)|}{S_{\text{ref}}} &= 10 \log \frac{\epsilon(f)}{\epsilon_{\text{ref}}} - 40 \log \frac{f}{f_{\text{ref}}} \\ &\quad + 10 \log \frac{c_p \epsilon_{\text{ref}}}{8\pi^3 \rho S_{\text{ref}}^2 f_{\text{ref}}^4}, \end{aligned} \quad (\text{C.9})$$

where  $S_{\text{ref}} = 1 \text{ m}^3/\text{Hz}$ ,  $\epsilon_{\text{ref}} = 1 \text{ J/Hz}$ , and  $f_{\text{ref}} = 1 \text{ Hz}$ . For ice with  $c_p = 4 \text{ km/s}$  and  $\rho = 930 \text{ kg/m}^3$ , Eq. (C.9) becomes

$$L_s = L_\epsilon - 40 \log \frac{f}{f_{\text{ref}}} - 18, \quad (\text{C.10})$$

where  $L_s$  is the source level in dB re  $1 \text{ m}^3/\text{Hz}$ , and  $L_\epsilon$  is the radiated energy level in dB re  $1 \text{ J/Hz}$ . The relationship between the radiated energy and velocity can be obtained by substituting Eq. (C.7) into Eq. (C.9).

$$\begin{aligned} 10 \log \frac{\epsilon(f)}{\epsilon_{\text{ref}}} &= 20 \log \frac{|\dot{u}_{r_s}(r_s, f)|}{\dot{u}_{\text{ref}}} + 10 \log \frac{8\pi \rho c_p r_{\text{ref}}^2 \dot{u}_{\text{ref}}^2}{\epsilon_{\text{ref}}} \\ &\quad + 20 \log \frac{r}{r_{\text{ref}}}, \end{aligned} \quad (\text{C.11})$$

where  $\dot{u}_{\text{ref}} = 1 \text{ } \mu\text{m s}^{-1} \text{ Hz}^{-1}$ , and  $r_{\text{ref}} = 1 \text{ m}$ . The last term on the right-hand side of the equation is the transmission loss

$$\text{TL} = -20 \log \frac{r_s}{r_{\text{ref}}}, \quad (\text{C.12})$$

which takes the spherical spreading loss in free space into account. Equation (C.11) then becomes

$$L_{\dot{u}_{r_s}} = L_\epsilon + \text{TL} - 20, \quad (\text{C.13})$$

where  $L_{\dot{u}_{r_s}}$  is the velocity level in dB re  $1 \text{ } \mu\text{m s}^{-1} \text{ Hz}^{-1}$ , so that the radiated energy level and the velocity level are directly related.

This result can be generalized for a waveguide by rewriting Eqs. (5) and (6) as

$$\dot{u}_m(r, z, f) = \frac{(2\pi f)^2 S(f)}{4\pi c_p} \left[ \frac{4\pi c_p}{(2\pi f)^2} G_{\dot{u},m}(r, z, f) \right], \quad (\text{C.14})$$

$$\dot{w}_m(r, z, f) = \frac{(2\pi f)^2 S(f)}{4\pi c_p} \left[ \frac{4\pi c_p}{(2\pi f)^2} G_{\dot{w},m}(r, z, f) \right]. \quad (\text{C.15})$$

Using Eq. (C.8), we have

$$|\dot{u}_m(r, z, f)|^2 = \frac{\epsilon(f)}{8\pi \rho c_p} \left| \frac{4\pi c_p}{(2\pi f)^2} G_{\dot{u},m}(r, z, f) \right|^2, \quad (\text{C.16})$$

$$|\dot{w}_m(r, z, f)|^2 = \frac{\epsilon(f)}{8\pi \rho c_p} \left| \frac{4\pi c_p}{(2\pi f)^2} G_{\dot{w},m}(r, z, f) \right|^2. \quad (\text{C.17})$$

Equations relating received velocity level to source energy level and transmission loss similar to Eq. (C.13) can be obtained by taking the log of both sides of the previous two equations,

$$L_{\dot{u}} = L_\epsilon + \text{TL}_{\dot{u}} - 20, \quad (\text{C.18})$$

$$L_{\dot{w}} = L_\epsilon + \text{TL}_{\dot{w}} - 20, \quad (\text{C.19})$$

where  $L_{\dot{u}}$  and  $L_{\dot{w}}$  are horizontal and vertical velocity levels in dB re  $1 \mu\text{m s}^{-1} \text{Hz}^{-1}$ . The transmission losses in the horizontal and vertical particle velocities are given by

$$\text{TL}_{\dot{u}} = -20 \log \left[ \left| \frac{4\pi c_p}{(2\pi f)^2} G_{\dot{u},m}(r, z, f) \right|^{-1} / r_{\text{ref}} \right], \quad (\text{C.20})$$

$$\text{TL}_{\dot{w}} = -20 \log \left[ \left| \frac{4\pi c_p}{(2\pi f)^2} G_{\dot{w},m}(r, z, f) \right|^{-1} / r_{\text{ref}} \right] \quad (\text{C.21})$$

which are identical to Eq. (17) for  $r_{\text{ref}} = 1 \text{ m}$ .

In general, this relationship is valid in the frequency domain only, since, in the time domain, each frequency response is weighted by the source spectrum and synthesized by the Fourier integral,

$$\dot{u}(r, z, t) = \int_{-\infty}^{\infty} S(f) G_{\dot{u}}(r, z, f) e^{-i2\pi ft} df. \quad (\text{C.22})$$

The source spectrum in a given frequency band  $f_1 < f < f_2$  can be expressed as

$$S(f) \simeq A(\chi) \tilde{S}(f), \quad (\text{C.23})$$

if the source spectrum retains the same shape  $\tilde{S}(f)$  with varying amplitude  $A$  that is a function of the source parameter  $\chi$ . The velocity in time domain after filtering can be expressed as

$$\dot{u}(r, z, t) \simeq A(\chi) \int_{f_1}^{f_2} \tilde{S}(f) G_{\dot{u}}(r, z, f) e^{-i2\pi ft} df. \quad (\text{C.24})$$

By taking the log of both sides,

$$L_{\dot{u}}(\chi) \simeq L_A(\chi) + \tilde{L}_{\dot{u}}, \quad (\text{C.25})$$

where

$$L_A(\chi) = 10 \log A^2(\chi), \quad (\text{C.26})$$

$$\tilde{L}_{\dot{u}} = 10 \log \left| \int_{f_1}^{f_2} \tilde{S}(f) G_{\dot{u}}(r, z, f) e^{-i2\pi ft} df \right|^2. \quad (\text{C.27})$$

Equation (C.25) shows that velocity level  $L_{\dot{u}}(\chi_1)$  can be scaled to velocity level  $L_{\dot{u}}(\chi_2)$  by

$$L_{\dot{u}}(\chi_2) \simeq L_{\dot{u}}(\chi_1) + [L_A(\chi_2) - L_A(\chi_1)]. \quad (\text{C.28})$$

Furthermore, substitution of Eq. (C.23) into Eq. (C.8) shows that

$$L_A(\chi_2) - L_A(\chi_1) = L_\epsilon(\chi_2) - L_\epsilon(\chi_1). \quad (\text{C.29})$$

Therefore, Eq. (C.28) can be changed to

$$L_{\dot{u}}(\chi_2) \simeq L_{\dot{u}}(\chi_1) + [L_\epsilon(\chi_2) - L_\epsilon(\chi_1)], \quad (\text{C.30})$$

where the velocity level is simply expressed in terms of the change in source energy level.

For surface cracks  $\chi = h$ , and for impactors  $\chi = s_0$ , where  $s_0$  is the permanent volume injection by an impactor

as defined in Appendix C.2. The differences between the energy spectra can either be obtained from Figs. 5 and 6, or

$$L_\epsilon(h_1) - L_\epsilon(h_2) = 80 \log \frac{h_1}{h_2}, \quad h \leq 250 \text{ m}, \quad (\text{C.31})$$

for surface cracks, and

$$L_\epsilon(s_{0,1}) - L_\epsilon(s_{0,2}) = 20 \log \frac{s_{0,1}}{s_{0,2}}, \quad r_m \leq 10 \text{ m}, \quad (\text{C.32})$$

for impactors when  $f \leq 4 \text{ Hz}$ , as shown in Appendices C.1 and C.2. Equation (C.32) can also be expressed in terms of the impactor radius  $r_m$ ,

$$L_\epsilon(r_{m,1}) - L_\epsilon(r_{m,2}) = 60 \log \frac{r_{m,1}}{r_{m,2}}, \quad r_m \leq 10 \text{ m}, \quad (\text{C.33})$$

given the density  $\rho_m$  and the impact velocity  $v_m$  of an impactor.

The ambient noise levels in Eqs. (26) and (27) can also be scaled by source energy level

$$\langle |S(f)|^2 | \chi \rangle = A^2(\chi) \langle |\tilde{S}(f)|^2 \rangle, \quad (\text{C.34})$$

based on Eq. (C.23). Then using Eqs. (23) and (26), we have

$$\text{NL}_{\dot{u}}(\chi_2) \simeq \text{NL}_{\dot{u}}(\chi_1) + [L_\epsilon(\chi_2) - L_\epsilon(\chi_1)], \quad (\text{C.35})$$

so that the velocity level and the noise level can be scaled by the same term for a given change in source energy level.

### C.1. Radiated energy spectra from tensile cracks

The radiated energy spectra for tensile cracks can be estimated in a spherical coordinate system  $(r_s, \theta, \varphi)$  with corresponding particle velocity components  $\dot{u}_{r_s}, \dot{u}_\theta, \dot{u}_\varphi$  (Haskell, 1964). Assuming that the radial velocity is compressional and the other components are due to shear,

$$\begin{aligned} \epsilon_{c_p}(f) &= 2\rho c_p \int_0^{2\pi} \int_0^\pi |\dot{u}_{r_s}(f)|^2 r_s^2 \sin\theta \, d\theta \, d\varphi, \\ \epsilon_{c_s}(f) &= 2\rho c_s \int_0^{2\pi} \int_0^\pi (|\dot{u}_\theta(f)|^2 + |\dot{u}_\varphi(f)|^2) r_s^2 \\ &\quad \times \sin\theta \, d\theta \, d\varphi, \end{aligned} \quad (\text{C.36})$$

where

$$\begin{aligned} 4\pi c_s r_s \dot{u}_{r_s} &= \frac{c_s}{c_p} I_{c_p} \left[ 1 - 2 \left( \frac{c_s}{c_p} \right)^2 + 2 \left( \frac{c_s}{c_p} \right)^2 \sin^2\theta \sin^2\varphi \right], \\ 4\pi c_s r_s \dot{u}_\theta &= I_{c_s} \sin 2\theta \sin^2\varphi, \\ 4\pi c_s r_s \dot{u}_\varphi &= I_{c_s} \sin\theta \sin 2\varphi, \end{aligned} \quad (\text{C.37})$$

$$I_{c_p}(t) = D_0 h \int_0^h \ddot{D} \left( \tau_p - \frac{\eta}{v} \right) d\eta,$$

$$I_{c_s}(t) = D_0 h \int_0^h \ddot{D} \left( \tau_s - \frac{\eta}{v} \right) d\eta,$$

$$\begin{aligned}\tau_p &= t - \frac{d}{c_p}, \\ \tau_s &= t - \frac{d}{c_s},\end{aligned}\quad (\text{C.38})$$

and  $d$  is the distance from the instantaneous opening position of the propagating crack to the receiver position. Since  $d \gg h$  we take  $d$  to be a time-invariant constant measured from the center of the completed crack. This assumption is consistent with monopole radiation, which is expected on average, and enables analytic evaluation of  $I_{c_{p,s}}$ .

The total radiated energy spectrum  $\epsilon(f)$  is the sum of the compressional wave energy spectrum  $\epsilon_{c_p}(f)$  and the shear wave energy spectrum  $\epsilon_{c_s}(f)$ .  $D(t)$  is the source shape function that satisfies the initial and final conditions

$$\begin{aligned}D(t) &= 0, \quad t < 0, \\ D(t) &\rightarrow 1, \quad t \rightarrow \infty.\end{aligned}\quad (\text{C.39})$$

We use the Haskell source model characterized by a ramp function as shown in Fig. C.1. The relative change of the energy spectrum as a function of crack depth is independent of this choice.

We also assume that the crack opening time  $\tau$  is the same as the crack propagation time  $T = h/v$ . Under these assumptions,

$$\begin{aligned}I_{c_{p,s}}(f) &= i \frac{2D_0 h^2}{T} \text{sinc}(Tf) \sin(\pi Tf) e^{-i2\pi f(d/c_{p,s}+T)}, \\ |I_{c_{p,s}}(f)| &\equiv |I(f)| = \frac{2D_0 h^2}{T} |\text{sinc}(Tf) \sin(\pi Tf)|, \\ \epsilon_{c_p}(f) &= |I(f)|^2 \frac{2\pi \rho c_p}{(4\pi c_s)^2 \xi^2} \left(4 - \frac{14}{3\xi^2}\right), \\ \epsilon_{c_s}(f) &= |I(f)|^2 \frac{2\pi \rho c_s}{(4\pi c_s)^2} \frac{37}{15},\end{aligned}\quad (\text{C.40})$$

where  $\text{sinc}(x) = \sin(\pi x)/(\pi x)$ .

We employ an equivalent volume injection source that has the same total radiated energy spectrum as a tensile crack by assuming

$$S(f) = i \frac{2D_0 h^2}{T} \text{sinc}(Tf) \sin(\pi Tf) e^{-i2\pi fT}$$

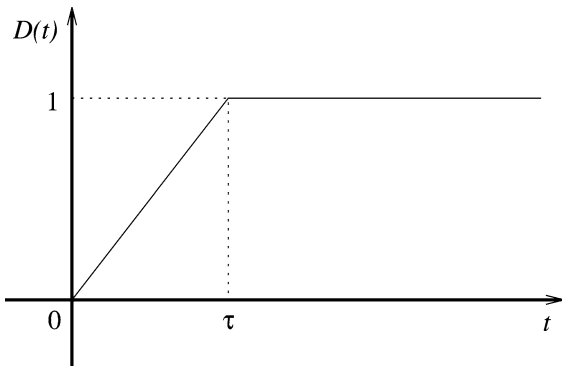


Fig. C.1. The source shape function  $D(t)$  for Haskell source model.  $\tau$  is the opening time of a surface crack.

$$\times \left[ \frac{\xi}{64\pi^4 f^4} \left\{ \frac{1}{\xi} \left( 4 - \frac{14}{3\xi^2} \right) + \frac{37}{15} \right\} \right]^{1/2}. \quad (\text{C.41})$$

Since  $\epsilon(f)$  is proportional to  $|I(f)|^2$ , the overall behavior of the source spectrum can be understood by analyzing the behavior of  $|I(f)|^2$ , where  $\rho I(f)$  is the Fourier transform of the rate of change of mass outflow from the source.

The frequency dependent characteristics of  $|I(f)|^2$  are determined by  $\text{sinc}^2(Tf) \sin^2(\pi Tf)$ , and its behavior with the 3-dB bandwidth is plotted in Fig. 4. Given the surface crack depth, the radiated energy level is

$$L_\epsilon = 10 \log \frac{\epsilon(f)}{\epsilon_{\text{ref}}} \sim 20 \log |\text{sinc}(Tf)| + 20 \log |\sin(\pi Tf)|, \quad (\text{C.42})$$

where the symbol  $\sim$  indicates “proportional to.”

For frequencies below the 3-dB bandwidth,  $\text{sinc}(Tf) \simeq 1$ ,  $\sin(\pi Tf) \simeq \pi Tf$ , so that

$$L_\epsilon \sim 20 \log(\pi Tf), \quad (\text{C.43})$$

which characterizes an energy spectrum that increases by 20 dB/decade.

For frequencies above the 3-dB bandwidth,  $\text{sinc}(Tf) \sim (\pi Tf)^{-1}$ , so that

$$L_\epsilon \sim -20 \log(\pi Tf), \quad (\text{C.44})$$

which characterizes an energy spectrum with rapid sinusoidal oscillation and a trend that falls off by 20 dB/decade.

The amplitude of the energy spectrum depends on the crack depth. By taking Eq. (3) into account, the peak of the energy spectral density

$$\epsilon(f)_{\text{max}} \sim |I(f)|_{\text{max}}^2 \sim \frac{D_0^2 h^4}{T^2} \sim D_0^2 h^2 \sim h^6,$$

follows a sixth power law in  $h$  so that the maximum energy level is

$$L_{\epsilon, \text{max}} \sim 60 \log \frac{h}{h_{\text{ref}}}, \quad (\text{C.45})$$

where  $h_{\text{ref}} = 1$  m. But this peak value varies with frequency as a function of crack depth  $h$ , as shown in Fig. 5.

The energy spectra for frequencies below the 3-dB bandwidth show greater differences across  $h$  than those found by comparing the spectral peaks since

$$\epsilon(f) \sim \frac{D_0^2 h^4}{T^2} |\text{sinc}(Tf) \sin(\pi Tf)|^2 \sim D_0^2 h^4 \sim h^8$$

leads to an eighth power law in  $h$  and the corresponding energy level functionality

$$L_\epsilon \sim 80 \log \frac{h}{h_{\text{ref}}}, \quad (\text{C.46})$$

from which Eq. (C.31) can be obtained.

When  $f < 1/T$  the source spectrum can also be approximated as

$$S(f) \simeq 2\pi i D_0 h^2 f \left[ \frac{\xi}{64\pi^4 f^4} \left\{ \frac{1}{\xi} \left( 4 - \frac{14}{3\xi^2} \right) + \frac{37}{15} \right\} \right]^{1/2}, \quad (\text{C.47})$$

so that the amplitude of the source spectrum in Eq. (C.23) can be approximated as

$$A(h) = D_0 h^2 \sim h^4,$$

which explicitly shows its dependence on crack depth.

### C.2. Radiated energy spectra from impactors

To estimate the radiated energy spectrum of an impactor, we base our estimation on the impact-explosion analogy.

Given the kinetic energy  $E_K$  of an impactor, the seismic efficiency of the impact is defined as

$$\eta_s = \frac{E_S}{E_K}, \quad (\text{C.48})$$

where  $E_S$  is the total radiated seismic energy. The seismic efficiency typically varies from  $10^{-3}$  to  $10^{-5}$  with the most commonly accepted value of  $10^{-4}$  (Schultz and Gault, 1975; Melosh, 1989).

In underground explosions of spherical radiation, permanent volume injection is related to the total radiated seismic energy by

$$E_S = \frac{\pi^2 \rho f_c^3 s_0^2}{2c_s}, \quad (\text{C.49})$$

where  $s_0$  is the permanent volume injection measured in the elastic regime from the explosion. The corner frequency  $f_c$  is given by

$$f_c = \frac{c_s}{\pi R_e} \quad (\text{C.50})$$

in the model employed by Denny and Johnson (1991). It is worth noting that the corner frequencies in both surface cracks and impactors are proportional to the ratio of the wave speed in the medium and the characteristic length of the seismo-acoustic source. When the impact velocity of the impactor onto a rocky target is larger than a few kilometers per second, the elastic radius  $R_e$  can be assumed as

$$R_e \simeq 20r_m, \quad (\text{C.51})$$

where  $r_m$  is the radius of an impactor (Ahrens and O'Keefe, 1977; Melosh, 1989).

The permanent volume injection from an impactor can be estimated using Eqs. (C.48)–(C.51),

$$s_0 = \left[ \frac{2c_s E_S}{\pi^2 \rho f_c^3} \right]^{1/2} = \left[ \frac{1.2 \times 10^4 \times \eta_s \rho_m v_m^2}{\rho c_s^2} \right]^{1/2} \mathcal{V}_m, \quad (\text{C.52})$$

where  $\rho_m$ ,  $v_m$ , and  $\mathcal{V}_m$  are the density, impact velocity, and volume of the impactor.

The source spectrum and the total radiated energy spectrum are given by (Denny and Johnson, 1991)

$$S(f) = \frac{s_0 f_c^2}{i2\pi f [(f_c^2 - f^2) + 2if_c f / \xi]} = \frac{s_0}{i2\pi f \{ [1 - (f/f_c)^2] + i2f/(\xi f_c) \}}, \quad (\text{C.53})$$

$$\epsilon(f) = \frac{2\pi\rho}{c_p} \frac{s_0^2 f^2}{\{1 - (f/f_c)^2\}^2 + (2f/(\xi f_c))^2}. \quad (\text{C.54})$$

As can be observed in Eq. (C.54), the energy spectral density at the corner frequency, slightly above the frequency of the peak, is

$$\epsilon(f_c) \sim s_0^2 f_c^2 \sim r_m^4,$$

which shows a fourth power law in  $r_m$  that leads to the energy level dependence

$$L_{\epsilon, f_c} \sim 40 \log(r_m/r_{m,\text{ref}}), \quad (\text{C.55})$$

given  $\rho_m$  and  $v_m$  for the impactor, where  $r_{m,\text{ref}} = 1$  m. Since  $\epsilon(f) \sim f^2$  if  $f \ll f_c$ , and  $\epsilon(f) \sim f^{-2}$  if  $f \gg f_c$ , the slope of the energy spectrum follows the same laws as surface cracks above and below the 3-dB bandwidth.

For  $f$  below the 3-dB bandwidth,

$$S(f) \simeq \frac{s_0}{i2\pi f} \sim r_m^3,$$

so that the source amplitude function in Eq. (C.23) can be expressed as

$$A(s_0) = s_0.$$

The radiated energy spectrum can then be approximated as

$$\epsilon(f) \simeq \frac{2\pi\rho}{c_p} s_0^2 f^2 \sim r_m^6,$$

with energy spectral level following the dependence

$$L_\epsilon = 10 \log \frac{\epsilon(f)}{\epsilon_{\text{ref}}} \sim 20 \log \frac{s_0}{s_{0,\text{ref}}} \sim 60 \log \frac{r_m}{r_{m,\text{ref}}}, \quad (\text{C.56})$$

where  $s_{0,\text{ref}} = 1$  m<sup>3</sup>. The difference between the energy spectral levels for various impactors can be determined by Eqs. (C.32) and (C.33).

The radiated energy levels for impactors of various radii are given in Fig. 6, assuming  $\rho_m = 3$  g/cm<sup>3</sup> and  $v_m = 20$  km/s. The seismic efficiency was assumed to be  $10^{-4}$ . The radiated energy spectrum can vary by  $\pm 10$  dB due to the uncertainty in the seismic efficiency.

## References

- Ahrens, T.J., O'Keefe, J.D., 1977. Equations of state and impact-induced shock-wave attenuation on the Moon. In: Roddy, D.J., Pepin, R.O., Merrill, R.B. (Eds.), *Impact and Explosion Cratering*. Pergamon, New York, pp. 639–656.
- Aki, K., Richards, P.G., 1980. *Quantitative Seismology*. Freeman, San Francisco.
- Anderson, J.D., Schubert, G., Jacobson, R.A., Lau, E.L., Moore, W.B., Sjogren, W.L., 1998. Europa's differentiated internal structure: inferences from four Galileo encounters. *Science* 281, 2019–2022.
- Anderson, O.L., 1963. A simplified method for calculating the Debye temperature from elastic constant. *J. Phys. Chem. Solids* 24, 909–917.
- Bierhaus, E.B., Chapman, C.R., Merline, W.J., Brooks, S.M., Asphaug, E., 2001. Pwyll secondaries and other small craters on Europa. *Icarus* 153, 264–276.
- Brekhovskikh, L.M., 1980. *Waves in Layered Media*, 2nd edition. Academic Press, New York.

- Brekhovskikh, L.M., Lysanov, Y., 1982. Fundamentals of Ocean Acoustics. In: Springer Ser. Electrophys., Vol. 8. Springer-Verlag, Berlin.
- Chen, C.-T., Millero, F.J., 1977. Speed of sound in seawater at high pressures. *J. Acoust. Soc. Am.* 62, 1129–1135.
- Chyba, C.F., Ostro, S.J., Edwards, B.C., 1998. Radar detectability of a subsurface ocean on Europa. *Icarus* 134, 292–302.
- Cooper, J.F., Phillips, C.B., Green, J.R., Wu, X., Carlson, R.W., Tamppari, L.K., Terrile, R.J., Johnson, R.E., Eraker, J.H., Makris, N.C., 2002. Europa exploration: science and mission priorities. In: Sykes, M.V. (Ed.), *The Future of Solar System Exploration, 2003–2013 Community Contributions to the NRC Solar System Exploration Decadal Survey*. In: *Astron. Soc. Pacific Conf. Ser.*, Vol. 272. Astronomical Society of the Pacific, California, pp. 217–252.
- Crawford, G.D., Stevenson, D.J., 1988. Gas driven water volcanism and the resurfacing of Europa. *Icarus* 73, 66–79.
- Denny, M.D., Johnson, L.R., 1991. The explosion seismic source function: models and scaling laws reviewed. In: Taylor, S.R., Patton, H.J., Richards, P.G. (Eds.), *Explosion Source Phenomenology*. In: *Geophys. Monograph*, Vol. 65. American Geophysical Union, pp. 1–24.
- Deschamps, F., Sotin, C., 2001. Thermal convection in the outer shell of large icy satellites. *J. Geophys. Res.* 106, 5107–5121.
- Farmer, D.M., Xie, Y., 1989. The sound generated by propagation cracks in sea ice. *J. Acoust. Soc. Am.* 85, 1489–1500.
- Frisk, G.V., 1994. *Ocean and Seabed Acoustics: A Theory of Wave Propagation*. Prentice Hall, Englewood Cliffs, NJ.
- Gagnon, R.E., Kieft, H., Clouter, M.J., 1988. Pressure dependence of the elastic constants of ice Ih to 2.8 kbar by Brillouin spectroscopy. *J. Chem. Phys.* 89, 4522–4528.
- Greeley, R., Chyba, C., Head, J.W., McCord, T., McKinnon, W.B., Pappalardo, R.T., 2003. Geology and geophysics of Europa. In: Bagenal, F., McKinnon, W.B., Dowling, T. (Eds.), *Jupiter: The Planet, Satellite, and Magnetosphere*. Submitted.
- Greenberg, R., 2002. Tides and the biosphere of Europa. *Am. Sci.* 90, 48–55.
- Greenberg, R., Geissler, P., Hoppa, G., Tufts, B.R., Durda, D.D., 1998. Tectonic processes on Europa: tidal stresses, mechanical response, and visible features. *Icarus* 135, 64–78.
- Haskell, N.A., 1964. Total energy and energy spectral density of elastic wave radiation from propagating faults. *Bull. Seismol. Soc. Am.* 54, 1811–1841.
- Hoppa, G.V., Tufts, B.R., Greenberg, R., Geissler, P.E., 1999. Formation of cycloidal features on Europa. *Science* 285, 1899–1902.
- Hunkins, K., 1960. Seismic studies of sea ice. *J. Geophys. Res.* 65, 3459–3472.
- Joset, A., Holtzschcher, J.-J., 1953. Étude des vitesses de propagation des ondes sismiques sur l'inlandsis du Groenland. *Ann. Geophys.* 9, 330–344.
- Khurana, K.K., Kivelson, M.G., Stevenson, D.J., Schubert, G., Russell, C.T., Walker, R.J., Polansky, C., 1998. Induced magnetic fields as evidence for subsurface oceans in Europa and Callisto. *Nature* 395, 777–780.
- Kim, J.S., 1989. Radiation from Directional Seismic Sources in Laterally Stratified Media with Application to Arctic Ice Cracking Noise. PhD thesis. Massachusetts Institute of Technology.
- Kivelson, M.G., Khurana, K.K., Russell, C.T., Volwerk, M., Walker, R.J., Zimmer, C., 2000. Galileo magnetometer measurements: a stronger case for a subsurface ocean at Europa. *Science* 289, 1340–1343.
- Kivelson, M.G., Khurana, K.K., Stevenson, D.J., Bennett, L., Joy, S., Russell, C.T., Walker, R.J., Zimmer, C., Polansky, C., 1999. Europa and Callisto: induced or intrinsic fields in a periodically varying plasma environment. *J. Geophys. Res.* 104, 4609–4625.
- Kovach, R.L., Chyba, C.F., 2001. Seismic detectability of a subsurface ocean on Europa. *Icarus* 150, 279–287.
- Kuperman, W.A., Ingenito, F., 1980. Spatial correlation of surface generated noise in a stratified ocean. *J. Acoust. Soc. Am.* 67, 1988–1996.
- Lange, M.A., Ahrens, T.J., 1983. The dynamic tensile strength of ice and ice-silicates mixtures. *J. Geophys. Res.* 88, 1197–1208.
- Leith, A.C., McKinnon, W.B., 1996. Is there evidence for polar wander on Europa? *Icarus* 120, 387–398.
- Lotze, W., 1957. Schallgeschwindigkeitsmessungen von Eis in Abhängigkeit von Druck und Temperatur. *Z. Geophys.* 23, 243–249.
- Makris, N.C., Dyer, I., 1986. Environmental correlates of pack ice noise. *J. Acoust. Soc. Am.* 79, 1434–1440.
- Makris, N.C., Dyer, I., 1991. Environmental correlates of Arctic ice-edge noise. *J. Acoust. Soc. Am.* 90, 3288–3298.
- McCammon, D.F., McDaniel, S.T., 1985. The influence of the physical properties of ice on reflectivity. *J. Acoust. Soc. Am.* 77, 499–507.
- McKinnon, W.B., 1999. Convective instability in Europa's floating ice shell. *Geophys. Res. Lett.* 26, 951–954.
- Medwin, H., Clay, C.S., 1998. *Fundamentals of Acoustical Oceanography*. Academic Press, Boston.
- Mellor, M., 1983. Mechanical behavior of sea ice. Technical Report Monograph 83-1. US Army Cold Regions Research & Engineering Laboratory.
- Melosh, H.H., 1989. Impact Cratering: A Geologic Process. In: *Oxford Monographs Geol. Geophys.*, Vol. 11. Oxford Univ. Press, New York.
- Miklowitz, J., 1978. *The Theory of Elastic Waves and Waveguides*. North-Holland, Amsterdam.
- Moore, J.C., 2000. Models of radar absorption in European ice. *Icarus* 147, 292–300.
- Muller, O., Muller, M.R., 1980. Near surface magma movements. In: *Proc. Lunar Planet. Sci. Conf.* 11th, 1979–1985.
- Nur, A., 1982. The origin of tensile fracture lineaments. *J. Struct. Geol.* 4, 31–40.
- Ojakangas, G.W., Stevenson, D.J., 1989. Thermal state of an ice shell on Europa. *Icarus* 81, 220–241.
- Orton, G.S., Spencer, J.R., Travis, L.D., Martin, T.Z., Tamppari, L.K., 1996. Galileo photopolarimeter-radiometer observations of Jupiter and the Galilean satellites. *Science* 274, 389–391.
- Pappalardo, R.T., Head, J.W., Greeley, R., Sullivan, R.J., Pilcher, C., Schubert, G., Moore, W.B., Carr, M.H., Moore, J.M., Belton, M.J.S., Goldsby, D.L., 1998. Geological evidence for solid-state convection in Europa's ice shell. *Nature* 391, 365–367.
- Pekeris, C.L., 1948. Theory of propagation of explosive sound in shallow water. *Geol. Soc. Am. Mem.* 27.
- Proctor Jr., T.M., 1966. Low-temperature speed of sound in single-crystal ice. *J. Acoust. Soc. Am.* 39, 972–977.
- Robin, G.Q., 1953. Measurements of ice thickness in Dronning Maud Land, Antarctica. *Nature* 171, 55–58.
- Robin, G.Q., 1958. Glaciology III, seismic shooting and related investigations. In: *Norwegian–British–Swedish Antarctic Expedition, 1949–1952, Scientific Results*, Vol. 5. Norsk Polarinstitut, Oslo.
- Schenk, P.M., 2002. Thickness constraints on the icy shells of the Galilean satellites from a comparison of crater shapes. *Nature* 417, 419–421.
- Schmidt, H., Tango, G., 1986. Efficient global matrix approach to the computation of synthetic seismograms. *Geophys. J. Roy. Astr. Soc.* 84, 331–359.
- Schultz, P.H., Gault, D.E., 1975. Seismic effects from major basin formation on the Moon and Mercury. *Moon* 12, 159–177.
- Shaw, G.H., 1986. Elastic properties and equation of state of high pressure ice. *J. Chem. Phys.* 84, 5862–5868.
- Spencer, J.R., Tamppari, L.K., Martin, T.Z., Travis, L.D., 1999. Temperatures on Europa from Galileo photopolarimeter-radiometer: nighttime thermal anomalies. *Science* 284, 1514–1516.
- Stewart, S.T., Ahrens, T.J., 1999. Correction to the dynamic tensile strength of ice and ice-silicate mixtures (Lange and Ahrens, 1983). In: *Proc. Lunar Planet. Sci. Conf.* 30th. Abstract 2037.
- Urlick, R.J., 1983. *Principles of Underwater Sound*, 3rd edition. McGraw-Hill, New York.
- Weeks, W.F., Cox, G.F.N., 1984. The mechanical properties of sea ice: a status report. *Ocean Sci. Eng.* 9, 135–198.

- Weertman, J., 1971a. Theory of water filled crevasses in glaciers applied to vertical magma transport beneath oceanic ridges. *J. Geophys. Res.* 76, 1171–1173.
- Weertman, J., 1971b. Velocity at which liquid filled cracks move in the Earth's crust or glaciers. *J. Geophys. Res.* 76, 8544–8553.
- Wilson, J.D., Makris, N.C., 2003. Ocean acoustic hurricane classification. *J. Acoust. Soc. Am.* Submitted.
- Wu, X., Bar-Sever, Y.E., Folkner, W.M., Williams, J.G., Zumberge, J.F., 2001. Probing Europa's hidden ocean from tidal effects on orbital dynamics. *Geophys. Res. Lett.* 28, 2245–2248.